
Training Hybrid Deep Quantum Neural Networks for Efficient Reinforcement Learning

Jie Luo

Anyon Computing Inc., USA

jluo@anyoncomputing.com

Jeremy Kulcsar

HSBC Quantum Technologies Group, Innovation & Ventures, HSBC, Hong Kong

jeremy.kulcsar@hsbc.com.hk

Xueyin Chen

Airbnb, Inc., USA

s.chen@airbnb.com

Georgios Korpas

HSBC Quantum Technologies Group, Innovation & Ventures, HSBC, Singapore

Department of Computer Science, Czech Technical University in Prague, Czechia

Archimedes Research Unit on AI, Data Science and Algorithms, Greece

georgios.korpas@hsbc.com.sg

Giulio Giaconi

HSBC Quantum Technologies Group, Innovation & Ventures, HSBC, United Kingdom

giulio.giaconi@hsbc.com

Abstract

Quantum circuits embed data in a Hilbert space whose dimensionality grows exponentially with the number of qubits, allowing even shallow parameterised quantum circuits (PQCs) to represent highly-correlated probability distributions that are costly for classical networks to capture. Reinforcement-learning (RL) agents, which must reason over long-horizon, continuous-control tasks, stand to benefit from this expressive quantum feature space, but only if the quantum layers can be trained jointly with the surrounding deep-neural components. Current gradient-estimation techniques (e.g., parameter-shift rule) make such hybrid training impractical for realistic RL workloads, because every gradient step requires a prohibitive number of circuit evaluations and thus erodes the potential quantum advantage. We introduce qtDNN, a tangential surrogate that locally approximates a PQC with a small differentiable network trained on-the-fly from the same minibatch. Embedding qtDNN inside the computation graph yields scalable batch gradients while keeping the original quantum layer for inference. Building on qtDNN we design hDQNN-TD3, a hybrid deep quantum neural network for continuous-control reinforcement learning based on the TD3 architecture. On the high-dimensional Humanoid-v4 benchmark, our agent reaches a test return that surpasses classical TD3, SAC and PPO baselines trained with identical compute. To our knowledge this is the first PQC-enhanced policy that matches or exceeds state-of-the-art classical performance on Humanoid. qtDNN has the potential to

reduce quantum-hardware calls significantly and is designed to be compatible with today’s NISQ devices. The method opens a path toward applying hybrid quantum models to large-scale RL and other gradient-intensive machine-learning tasks.

1 Introduction

Quantum computing has initially attracted significant attention for its potential to solve classically challenging problems by exploiting data representations in a Hilbert space that grows exponentially with the number of qubits, as discussed by Biamonte et al. [2017]. Machine learning (ML) is an application field that could benefit greatly from quantum computing, as patterns are learned from increasingly large datasets (cf. Vaswani et al. [2023], DeepSeek-AI et al. [2025b]) and more efficient methods are necessary to advance artificial intelligence (cf. Robison [2024], Samsi et al. [2023], Wells [2025]). Quantum machine learning (QML) aims at enhancing the efficiency and generalizability of learning beyond classical methods (see Table 1 in Biamonte et al. [2017] for known speedups of various subroutines). Although fault-tolerant quantum machines capable of running complex circuits without error are not yet available to exponentially accelerate computing with algorithms based on Harrow et al. [2009] or Brassard et al. [2000], the rapid development of noisy intermediate-scale quantum (NISQ) devices has inspired a new class of QML techniques designed to operate under noisy constraints (cf. Wang and Liu [2024]). On one hand, recent quantum supremacy experiments demonstrated that NISQ quantum devices can generate distributions where measured qubit states exhibit correlations that can not be simulated with reasonable classical compute (cf. Arute et al. [2019], Acharya et al. [2025], Gao et al. [2025]). On the other hand, a subfield of ML, reinforcement learning (RL) has become a central pillar of modern AI (cf. ACM [2025]), by estimating classical probability distributions that capture regularities in its interaction data (cf. Vaswani et al. [2023]), which allows an RL agent to refine its policy to attain high performance on target tasks (cf. Schulman et al. [2017], Haarnoja et al. [2018], DeepSeek-AI et al. [2025a]). Nontrivial highly correlated distributions seen in sampled output data (cf. Andersen et al. [2025]) from NISQ QPUs have the potential to better model complicated correlations in applications (cf. Lo et al. [2023], Huang et al. [2022], Vaswani et al. [2023]), allowing RL models to achieve higher rewards, data efficiency, and robustness. Recent work from Jin et al. [2025] has shown that SOTA quantum reinforcement learning (QRL) with PPO modified to incorporate parametrized quantum circuits (PQCs), could have similar performance as the classical baseline models from Raffin [2020] on simple reinforcement learning benchmarks in Towers et al. [2024]. This hybrid quantum machine learning is realized as a hybrid deep quantum neural network (hDQNN). In this setup, a classical deep neural network first maps the input into a vector of real numbers, those numbers become the control parameters fed to the downstream PQC during the forward pass. The input data to the PQC is encoded into the Hilbert space spanned by the N qubits, $\mathcal{H}_{Nq} \cong \mathbb{C}^{2^N}$. Low-dimensional classical input and projected (sampled) output act as bottleneck layers. QRL has shown a lot of promise when it comes to tackling tricky reinforcement learning tasks, especially those involving high-dimensional state and action (discrete and continuous) spaces. (cf. Dong et al. [2008], Paparo et al. [2014], Dunjko et al. [2017], Jerbi et al. [2021], Wu et al. [2025]) However, a significant barrier for applying hDQNNs to such high-dimensional problems is the cost of back-propagation through the PQC to update weights of classical DNNs before it.

Although methods exist for estimating gradients of a given PQC (cf. Wang and Liu [2024]), these can be impractical for real quantum hardware when the input and output dimensions are large as they require a large number of sequential quantum circuit measurements and are further incompatible with mini-batch updates due to the lack of parallel processing in physical QPUs. The lack of high-throughput training strategies compatible with NISQ hardware limits QRL’s practical performance and applicability to real-world tasks.

In this work, we introduce hDQNN-TD3, a hybrid quantum neural network architecture that approaches this bottleneck using a novel approach: a classical surrogate that we named qtDNN will approximate the PQC’s gradient updates on the backward pass. We demonstrate the hDQNN-TD3 model on the Humanoid-v4 reinforcement learning benchmark with better performance over the widely adopted classical SOTA counterparts. This paper is organized as follows: we will introduce the method that enables scalable training of hDQNN with classical DNNs around PQCs in Sec. 2. Following this, Sec. 3 will introduce hDQNN-TD3 for continuous variable RL tasks and show the experimental results from Humanoid-v4 demonstrating that hDQNN-TD3 outperforms comparable

classical methods as well as publicly reported models using SOTA RL architectures from Zhao [2024, 2023a,b]. The last Sec. 4 will discuss outlooks to train significantly larger models.

2 Neural PQC Tangential Approximation

2.1 Back-propagation and the quantum bottleneck

Modern machine learning methods are established with highly efficient backpropagation-based training: each operation in the computation graph supplies analytical Jacobians, so the loss can be differentiated w.r.t. millions of parameters and "backpropagated" through them with a single reverse pass. The updated parameters are used for a new forward pass, which creates a new differentiable loss. This process repeats until the loss reaches a set convergence condition.

On the other hand, hDQNNs are typically developed using PQCs to act as functional layers (QL) without learnable parameters. The described flow is typically interrupted by a QL¹. Fig. 1a shows the typical layout: a classical neural network **PreDNN** produces PQC control parameters \mathbf{q}_i , a QL outputting a bitstring \mathbf{q}_o after executing PQC S times, and a second classical neural network **PostDNN** maps \mathbf{q}_o to the final prediction. $d_{c\text{-link}}$ classical links directly connecting PreDNN and PostDNN are added on top of the QL. These direct links allow classical communication between the DNNs around the QL, to help the PostDNN properly handle the QL's sampled output.

It is however challenging to backpropagate loss efficiently through QLs. Unlike Gaussian re-parameterization layers, a PQC (and QL) has no closed-form gradient. Various strategies have been developed in recent years (cf. Wang and Liu [2024]). Most methods obtain the gradient vector of a PQC with respect to its input parameters by varying each input parameter and using repeated PQC executions to estimate its partial derivative with respect to each varied input. Such methods become quickly intractable as it must run $\mathcal{O}(I)$ extra circuits per output dimension, driving the hardware cost to $I \times O \times S \times N_b$ evaluations per mini-batch for the QL with I and Q input and output dimensions respectively (cf. Sec. A.1.2). Despite requiring many repeated measurements that scale with the size of input and output, methods based on direct PQC gradient estimation make it intrinsically unfeasible to batch-backpropagate in parallel, prohibiting efficient mini-batched training for a hDQNN, especially when it is applied to complex reinforcement learning.

2.2 qtDNN: a tangential PQC surrogate trained on-the-fly

We resolve this bottleneck by introducing the **qtDNN**, a quantum tangential space learning architecture that approximates the local behaviors of a QL with a classical DNN. The qtDNN is a small, differentiable surrogate network that locally mimics the PQC inside each mini-batch. It serves as a component of the hDQNN that substitutes the PQC whenever differentiability is needed.

The qtDNN is used during the training loop to provide a differentiable first-order approximation of PQC's behaviors, local to each minibatch during the backpropagation. Meanwhile, the forward inference pass goes through the QLs. To make training the qtDNN more efficient, we add a replay buffer (qtDNN-buffer) to each QL that stores the input, \mathbf{q}_i , and sampled output, \mathbf{q}_o , of the quantum layer as a pair, $(\mathbf{q}_i, \mathbf{q}_o)$, from each minibatch. This qtDNN-buffer is then used to train the qtDNN repeatedly with N_{qt} tiny-batches randomly sampled from this qtDNN-buffer. This accelerates qtDNN's convergence to a moving approximation to its target quantum layer (cf. Haarnoja et al. [2018]).

The update epoch is split in two stages (Fig. 1b–c):

1. **Surrogate fit:** From the sampled mini-batch $\mathcal{B} = \{(\mathbf{q}_i, \mathbf{q}_o)\}$ we draw N_{qt} tiny-batches to minimize a binary-cross-entropy between qtDNN(\mathbf{q}_i) and the observed bitstrings \mathbf{q}_o .
2. **Network update:** We freeze the qtDNN, replace the PQC by it in a surrogate model Q_{qt} that is otherwise identical to hDQNN, and run ordinary batched back-propagation to update the classical weights of the hDQNN.

¹QL: produces output from the expectation or most probable outcome over S shots of PQC, parametrized by its input, executed on simulator or physical QPU.

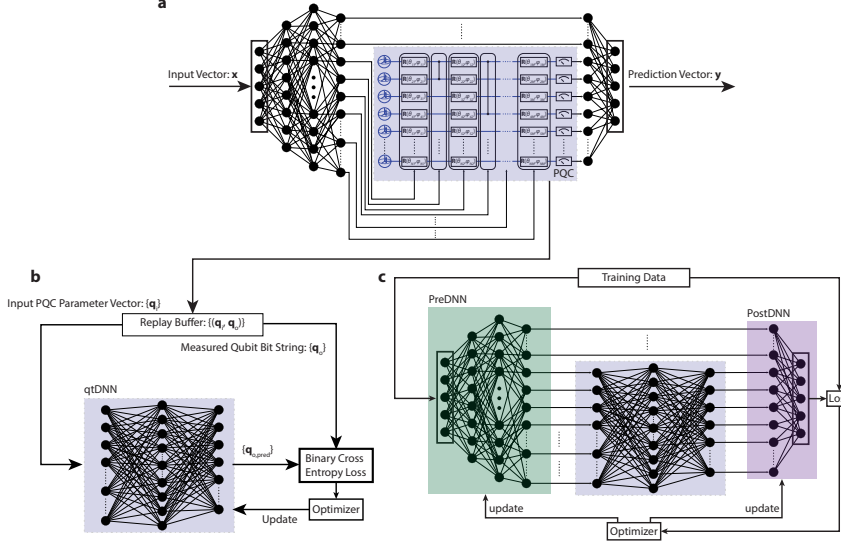


Figure 1: **a**, a typical hDQNN contains a PreDNN connected to a PostDNN via both d_c -link direct connections and a quantum layer realized as a parametrized quantum circuit. The hDQNN inferences through the training dataset and records $(\mathbf{x}, \mathbf{y}_{\text{pred}}, \mathbf{y}, \mathbf{q}_i, \mathbf{q}_o)$ of each forward pass into a buffer \mathcal{M} . In an update step, a batch, \mathcal{B} , of N_b entries is sampled from \mathcal{M} for updating hDQNN parameters. **b**, $\{(\mathbf{q}_i, \mathbf{q}_o)\}$ from \mathcal{M} is stored into a qtDNN Replay Buffer. N_{qt} tiny-batches, $\{\mathcal{B}_{\text{qt}}\}$, are sampled from \mathcal{B} are then used to update qtDNN towards approximating PQC in \mathcal{B} . **c**, the updated qtDNN is then used in the surrogate model Q_{qt} in this update step to facilitate the batched backpropagation of loss that are used to update the PreDNN and PostDNN with fixed qtDNN.

Because the qtDNN is itself a conventional MLP, gradients propagate without further quantum calls. The next subsection formalizes the approximation guarantee.

2.3 Local gradient fidelity of qtDNN

Intuitively, the PQC is a smooth function of its parameters over the small region explored by one mini-batch. A feed-forward MLP can capture its first-order behavior. Theorem 1 states this precisely:

Theorem 1 (Local gradient fidelity of qtDNN). *Let $Q : \mathbb{R}^d \rightarrow \mathbb{R}^k$ be the deterministic function realised by a PQC under the expectation over S shots, and suppose Q is continuously differentiable on an open set $\mathcal{U} \subset \mathbb{R}^d$. Fix a mini-batch $\mathcal{B} = \{x_i\}_{i=1}^{N_b} \subset \mathcal{U}$ lying in a closed ball of radius r centered at $\bar{x} = \frac{1}{N_b} \sum_i x_i$. For every pair of tolerances $(\varepsilon_1, \varepsilon_2) > 0$ there exists a feed-forward MLP $Q_\theta : \mathbb{R}^d \rightarrow \mathbb{R}^k$ such that:*

$$\max_{x \in \mathcal{B}} \|Q_\theta(x) - Q(x)\| \leq \varepsilon_1, \quad \max_{x \in \mathcal{B}} \|\nabla Q_\theta(x) - \nabla Q(x)\| \leq \varepsilon_2. \quad (1)$$

Consequently, if the PQC is replaced by Q_θ inside the computation graph during back-propagation, the mini-batch gradient with respect to any upstream parameter vector w is perturbed by at most an additive $O(\max(\varepsilon_1, \varepsilon_2))$ term.

The first inequality is simply the qtDNN learning to approximate the PQC's outputs correctly, while the second one shows that it learns to approximate the gradient of the PQC had it been differentiable i.e. approximate its effect during the backpropagation.

Intuition behind the proof. Because the mini-batch \mathcal{B} lies inside a small radius- r ball, Q is well-approximated by its first-order Taylor expansion around the centre \bar{x} . Thus, we (i) approximate the first-order Taylor polynomial $P(x) := Q(\bar{x}) + J_Q(\bar{x})(x - \bar{x})$ over \mathcal{B} by an MLP Q_θ , and (ii) use Lipschitz bounds on the second derivative of Q to control the Taylor remainder and its gradient. Replacing the PQC by that MLP therefore changes (i) forward activations by at most ε_1 and (ii) their Jacobian by at most ε_2 , which in turn perturbs the gradient flowing into earlier layers by the same order of magnitude. See Appendix A.2 for full details.

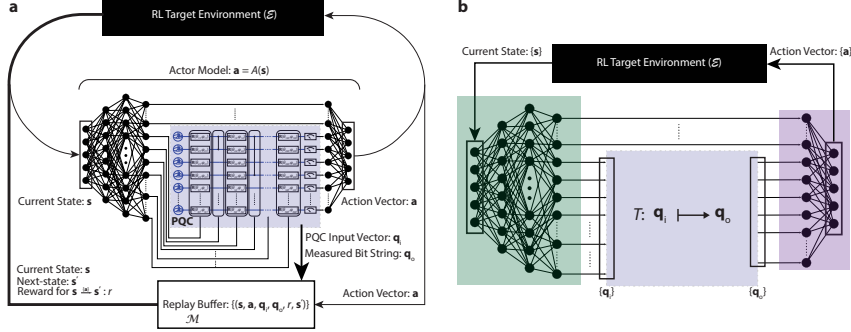


Figure 2: **a**, the typical exploration flow for the Agent to interact with the reinforcement learning objective’s target environment, \mathcal{E} , and obtain experience data to be stored in the replay buffer, \mathcal{M} . **b**, the particular modular model architecture used for the Actor Model, A , that allows the intermediate mapping T that maps its input vector q_i to q_o to be implemented differently without changing the rest of the model design. This allows comparing learning performance of different quantum and classical implementations fairly.

3 Quantum Reinforcement Learning

3.1 Problem set-up and motivation

We now instantiate the qtDNN surrogate inside a continuous-control agent (Fig. 2a). The target task is Humanoid-v4 ($d_{\text{obs}} = 376$, $d_{\text{act}} = 17$), a long-horizon MuJoCo benchmark considered challenging for both classical and quantum methods (Towers et al. [2024]). Classical baselines trained with identical compute on public HuggingFace repositories obtain final episode returns $\text{PPO} \approx 685$, $\text{SAC} \approx 5\,742$, $\text{TD3} \approx 5\,306$ (Zhao [2024], Zhao [2023a], Zhao [2023b]). We also saw that the best seed of our hybrid agent surpasses all three with 6 011 (see §3.5.1).

Actor design. The actor consists of a classical pre-network PreDNN, a middle block T , and a post-network PostDNN (Fig. 2b). We instantiate T as:

1. PQC (our hDQNN-TD3 model),
2. fully-connected (FC),
3. random bit generator (RBG), or
4. all-zero layer (OL)

to create a controlled ablation.

3.2 hDQNN-TD3 overview

We start from Twin-Delayed DDPG (TD3) because it is competitive yet simple. As the Actor Model is what drives the actions, a more generalizable Actor Model will directly impact the performance. Therefore, the original TD3 critic remains classical, only the actor contains the PQC (or its surrogate). The qtDNN is trained inside each mini-batch to approximate the PQC locally, enabling standard batched back-propagation through the whole actor. We call the resulting model **hDQNN-TD3**. Fig. 2 sketches the interaction loop between the Agent and the classical environment \mathcal{E} .

For clarity we recap the four alternating phases that occur during training, the symbols follow the notation introduced in Subsec. 2.2.

1. Exploration. At every environment step the current state $s \in \mathcal{S}$ is encoded by the PreDNN. Its output is split into (i) classical bypass features $d_{\text{c-link}}$, and (ii) the control vector q_i that parameterises the PQC layer. Sampling the PQC yields the binary vector q_o , which the PostDNN transforms—together with the bypass features—into the continuous action $a \in \mathcal{A}$. Applying a in \mathcal{E} returns the next state s' , reward r , and a done flag. The transition tuple (s, a, q_i, q_o, r, s') is appended to the replay buffer \mathcal{M} .

Algorithm 1 HDQNN-TD3: TD3 actor with a PQC and qtDNN surrogate

Require: Environment \mathcal{E} , replay buffer \mathcal{M} , actor A (PQC inside), twin critics C_1, C_2 , target networks A', C'_1, C'_2 , update periods N_A , surrogate epochs N_{qt}

- 1: **for** episode = 1, 2, ... **do**
- 2: **collect experience:** interact using $\mathbf{a}_t = A(\mathbf{s}_t) + \mathcal{N}_t$, store $(\mathbf{s}_t, \mathbf{a}_t, r_t, \mathbf{s}_{t+1})$ in \mathcal{M}
- 3: **if** time to update **then**
- 4: Sample mini-batch \mathcal{B} of size N_b from \mathcal{M}
- 5: (a) **update qtDNN:** train surrogate A_{qt} for N_{qt} tiny-batches $\{(\mathbf{q}_i, \mathbf{q}_o)\} \in \mathcal{B}$
- 6: (b) **critic step:** TD target $y = r + \gamma \min_{j=1,2} C'_j(\mathbf{s}', A'(\mathbf{s}'))$; regress C_1, C_2 to y
- 7: **if** global step mod $N_A = 0$ **then**
- 8: (c) **actor step:** maximize $C_1(\mathbf{s}, A_{\text{qt}}(\mathbf{s}))$ w.r.t. classical actor parameters
- 9: (d) **target update:** $\theta' \leftarrow \tau\theta + (1 - \tau)\theta'$
- 10: **end if**
- 11: **end if**
- 12: **end for**

2. qtDNN update. After \mathcal{M} holds at least N_b transitions we sample a mini-batch $\mathcal{B} \subset \mathcal{M}$. For every PQC in the Actor we collect the pairs $(\mathbf{q}_i, \mathbf{q}_o)$ of the batch and train its qtDNN surrogate with N_{qt} tiny-batches (from the same collection) using binary-cross-entropy. This freezes the qtDNNs for the remainder of the epoch.

3. Critic update (TD learning). With qtDNNs fixed, the surrogate Actor A_{qt} provides target actions $\hat{\mathbf{a}} = A_{\text{qt}}(\mathbf{s}')$. The two critics minimize the TD-error $\epsilon_{\text{TD}} = \|r + \gamma C_t(\mathbf{s}', \hat{\mathbf{a}}) - C(\mathbf{s}, \mathbf{a})\|^2$ as in TD3, using the loss averaged over \mathcal{B} .

4. Actor update. Every N_A critic steps we update the classical parameters of the Actor by maximizing $C(\mathbf{s}, A_{\text{qt}}(\mathbf{s}))$ through standard back-propagation that now flows through the differentiable qtDNN, thereby avoiding expensive parameter-shift evaluations of the PQC. Target networks C_t and A_t are softly updated with rate τ .

Algorithm 1 exposes the training loop pseudo code for hDQNN-TD3.

Moreover, Fig. 6 in Appendix D.2 details the data flow inside one update epoch, making explicit which parameters are optimized at which stage.

3.3 Quantum–classical instantiation details

The actor’s middle block T is a 10-qubit, 10-layer PQC. Each layer applies parameterized single-qubit rotations followed by at most one CZ entangler, and all controls come from the preceding PreDNN. Concretely:

- The input data is encoded in the controlling parameters $\{\theta_{ij}, \phi_{ij}, p_j, k_j\}$.
- $N = 10$ qubits, initialized in $|0\rangle^{\otimes N}$.
- $M = 10$ successive layers of gates.
- **Single-qubit stage.** For layer j and qubit i we apply $\mathbf{R}(\theta_{ij}, \phi_{ij})$, where $\theta_{ij}, \phi_{ij} \in [0, 2\pi)$ are two outputs of PreDNN. Across the layer this uses $2N$ neurons.
- **Entangling stage.** The same layer chooses a control–target pair $(p_j, k_j) \in \{0, \dots, N-1\}^2$ by rounding two additional PreDNN outputs and applies a CZ gate if $p_j \neq k_j$ (identity otherwise).
- Hence PreDNN provides $(2N + 2)M = 220$ real controls per actor forward pass.

All remaining architectural details², including qtDNN width ($L_h = 2048$), critic topology, learning rates, and exploration noise, are listed in Table 1, where α is the learning rate and the Critic follows the structure from Lillicrap et al. [2019].

²mini-batch size $N_b = 2^8$, actor update frequency $N_A = 2$.

Table 1: hDQNN Reinforcement Learning Model Configuration for Humanoid-v4 Problem

Components	DNN Design			Hyperparameters		
	Layers	Activation	N, M	$d_{\text{c-link}}$	α	γ
PreDNN	[376,256,230]	Leaky ReLU		10	$3e^{-4}$	$5e^{-3}$
qtDNN	[220,2 048,10]	Leaky ReLU			$3e^{-4}$	
PQC			10,10			
PostDNN	[20,256,17]	Leaky ReLU		10	$3e^{-4}$	$5e^{-3}$
Critic	[[376,256],[273,256,1]]	Leaky ReLU			$3e^{-4}$	0.99
						$5e^{-3}$

3.4 Experimental protocol

We train each agent for up to 7 200 episodes ($\approx 750\,000$ timesteps) across four seeds.³

The qtDNN uses a single hidden layer of size $L_h = 2\,048$ and $N_{\text{qt}} = 32$ updates per actor step. Other parameters are exposed in Table 1. PPO/SAC/TD3 baselines follow the best Hugging Face RL models on official Gymnasium Humanoid-v4 benchmark and consume the same number of steps to ensure a fair comparison.

Ablation. For the ablation in §3.5.2 we keep the same total number of environment episodes and we note that there is an error rate $\sim 10^{-3}$ associated with each PQC gate. Within the same architecture, we run the experiment for an FC layer, an RBG layer, and the PQC layer across $n_{\text{qubits}} \in \{5, 10\}$ and $n_{\text{shots}} \in \{100, 1\,000\}$. We omit the $(n_{\text{qubits}}, n_{\text{shots}}) = (5, 100)$ configuration because the run got impractically slow for some seeds (see Appendix A.1 for more details on limitations). A single-qubit setting would behave almost classically, whereas circuits with more than ≈ 20 qubits can trigger peaks above 30 GB in GPU memory, leaving too little head-room on the 40 GB GPU (cf. §3, Google Quantum AI [2025]). Likewise, 10 shots are statistically insufficient and 10 000 shots yield negligible variance reduction relative to their cost.

3.5 Results

3.5.1 General performance

In the following part, we will observe the mean test return across training sessions. The test return is recorded by averaging episode rewards of 10 test episodes every 10 000 training steps (approximately 10 training episodes when the agent can constantly finish the whole 1 000 steps of an episode). The graphs show a 10-episode rolling average.

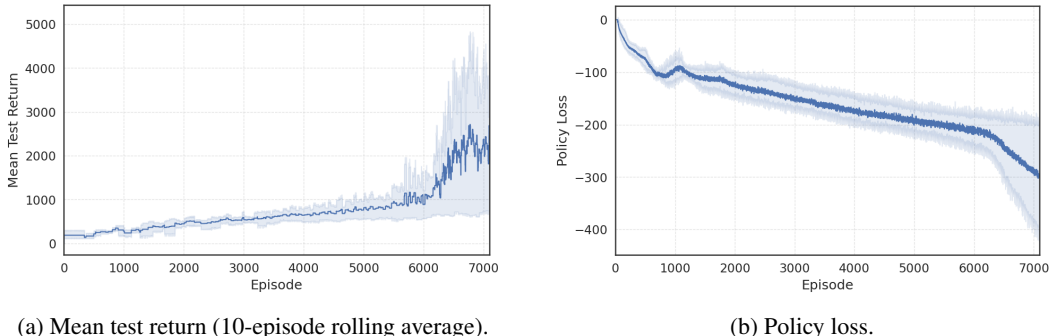


Figure 3: Learning dynamics of the hDQNN agent on Humanoid-v4. Shaded bands denote 95% confidence intervals across seeds.

³The horizon of 7,200 episodes balances limited compute resources against the large number of ablation variants we evaluate. A single longer-horizon run is provided in §3.5.1.

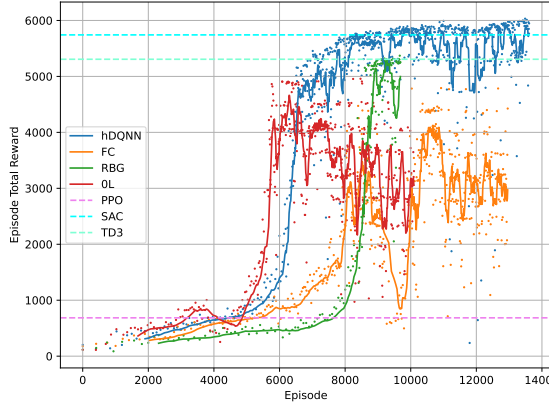


Figure 4: Mean test return (10-rolling average of each actor’s best seed).

Learning dynamics across seeds. Fig. 3 aggregates the four independent training runs across 7 200 episodes and reveals three salient trends. First, the mean test return (Fig. 3a) rises almost monotonically after the initial warm-up, surpassing the 10^3 mark around episode 3 000 and accelerating sharply once the actor has experienced 5 500 episodes. The shaded 95% confidence band widens in this late phase, indicating that one or two seeds surge ahead while the slower runs continue to improve, albeit more gradually. Second, the policy loss (Fig. 3b) mirrors this behavior in reverse: it drops rapidly to -100 during the first 1 000 episodes, then decays almost linearly to -200 before steepening again in tandem with the return surge. The broader confidence interval after episode 5 500 signals larger gradient magnitudes and increased exploration of high-return regions. Finally, the concurrent monotonic gain in return and decline in loss across all seeds confirms that the qtDNN surrogate supplies gradients of sufficient fidelity throughout training, while the late-stage divergence illustrates the head-room the quantum-enhanced actor can exploit once it enters the high-performance regime.

Best-seed comparison with benchmark. Fig. 4 contrasts the best seed of each actor variant over a longer 14 000-episode horizon.⁴ The hDQNN-TD3 actor (solid blue) climbs steeply after episode 5 500 and saturates near a $6 011 \pm 83$ return, surpassing the best seeds of classical TD3 (5 306), SAC (5 742) and PPO (685). Two additional aspects are noteworthy:

- *Sample-efficiency.* hDQNN-TD3 reaches the 3 000-return mark about 800 episodes earlier than its fully connected (FC) alternative, suggesting that the quantum layer helps discover high-value policies sooner.
- *Stability of convergence.* The hDQNN-TD3 curve flattens into a narrow band after episode 11 000, whereas the FC and RBG variants continue to exhibit larger oscillations, this indicates that the qtDNN surrogate supplies gradients of sufficient fidelity to stabilize late-stage policy refinement.

Overall, the figure supports our claim that, in the best case, a single well-tuned hDQNN seed can match the ceiling performance of the strongest classical baselines while requiring fewer interaction steps to get there.

3.5.2 Ablation study

Table 2 contrasts five actor variants at two training checkpoints⁵. The upper block (Episode 4 000) gives a mid-training snapshot. Already at this stage the 10-qubit, 1 000-shot PQC attains a mean

⁴For clarity the PPO, SAC and TD3 reference values from best Hugging Face RL models (Zhao [2024, 2023a,b]) on Gymnasium Humanoid-v4 are shown as horizontal dashed lines.

⁵Since the test return is noisy, we used the test return’s 10-episode rolling average across episodes to smoothen it and avoid recording misleading noise at the checkpoint.

Table 2: Ablation study on Humanoid-v4. Test returns are averaged over 4 seeds.

Episode	Layer	Shots	Qubits	Mean return	Best return	Time[min]	PQC calls
4 000	RBG	0	0	356.5 ± 219.1	545.3	39.8	0
4 000	FC	0	0	382.7 ± 167.5	603.6	27.4	0
4 000	PQC	100	10	470.8 ± 57.1	534.5	291.2	302 738
4 000	PQC	1000	5	521.3 ± 128.0	650.8	227.3	302 948
4 000	PQC	1000	10	678.7 ± 179.3	926.7	307.3	359 952
7 200	RBG	0	0	426.8 ± 114.5	545.0	105.9	0
7 200	FC	0	0	620.8 ± 393.8	1 207.8	89.8	0
7 200	PQC	100	10	517.8 ± 95.0	659.2	712.2	694 104
7 200	PQC	1000	5	1132.6 ± 1411.4	3 211.6	737.9	769 867
7 200	PQC	1000	10	768.9 ± 387.4	1 277.4	700.9	761 498

return of 678.7 ± 179.3 , and its best seed reaches 926.7, beating the FC by +296 (mean-to-mean) and the RBG by +322.

The lower block (Episode 7 200) captures late-training behavior. Here, the 5-qubit, 1 000-shot PQC leads with a mean return of $1 132.6 \pm 1 411.4$ and a best seed of 3 211.6, maintaining a +512 margin over FC and +706 over RBG. The larger 10-qubit variant still improves on FC by +149 despite its higher circuit cost.

Replacing the PQC with either an RBG or a deterministic FC layer consistently lowers final performance by hundreds of return points, confirming that the quantum layer contributes non-trivial modeling capacity rather than acting as a mere regulariser.

This consistent increase of performance between the FC and the PQC layer shows that the qtDNN is able to approximate the QL during back-propagation: the model is able to make use of the more complex representation of the QL during forward-prop and achieve a higher return, all while keeping stable gradients during back-propagation. Although not a direct experimental proof, this observation goes in the way of validating the local-tangent result of Theorem 1, i.e. $\|\nabla Q_\theta - \nabla Q\| \leq \varepsilon$ across the training.

3.5.3 Quantum calls

The PQC calls column from Table 2 shows how many quantum calls have been performed during the training. This number, K , is the same as the number of total steps the agent took during the training to explore its environment and populate the replay buffer, \mathcal{M} , for updating classical networks in off-policy training process. Each forward inference through the Actor Model makes one PQC call. Each PQC call to a quantum backend will return the estimated most probably bitstring from running identical PQC S times (shots) and obtaining bitstrings from measuring all qubits in each shot. Therefore, hDQNN trained with qtDNN makes the minimal number (K , the same as the number of inference) of PQC calls and $S \times K$ PQC executions on an expensive physical QPU. Meanwhile, alternative quantum hardware compatible gradient methods like parameter shifts require $\sim I \times Q \times N_b \times S \times K$ additional physical QPU runs over the training process for our QL with $I = 220$ dimensional input, $Q = 10$ dimensional output, and a mini-batch size of $N_b = 2^8$ in our cases.

4 Discussion

In this work, we proposed a novel way to efficiently train hDQNN compatible with NISQ quantum hardware, allowing for high-throughput mini-batch training using a surrogate classical neural network (qtDNN) to locally approximate and estimate gradients of the embedded quantum circuit for each mini-batch parameter update in off-policy reinforcement learning process. This method only requires expensive PQC calls in inference steps and therefore minimizes the number of expensive PQC calls in training significantly while still allows for efficient parallel mini-batch back-propagation to update classical weights. We further constructed hDQNN-TD3 model to learn complex, high-dimensional, and continuous-variable reinforcement learning tasks like Humanoid-v4 successfully with a final

reward score comparable to that of models with widely used SOTA architectures except the recently proposed MEow from Chao et al. [2024]. We further carried out ablation study by swapping the PQC to alternative classical layers and observed consistently better performance with hDQNN-TD3 against all comparable classical alternatives.

Therefore, training hDQNN with qDNN and inference with trained hDQNN on (noisy) quantum hardware offer a new route in reinforcement learning and AI research for addressing complicated real-world problems that are always stochastic, highly correlated, and even challenging to simulate classically. Further research in this direction could lead to novel models such as hDQNN-LLM where classical layers responsible for high-dimensional encoding and sampling in LLMs, such as DeepSeek-AI et al. [2025a], are replaced with QLs surrounded by classical DNNs to learn the strongly correlated distributions in natural language as hinted by Lo et al. [2023]. Moreover, the hDQNN-TD3 could be further developed to enhance models like NVIDIA [2025] in controlling advanced real-world robots.

Acknowledgements

This work has received partial funding from the European Union’s Horizon Europe research and innovation program under grant agreement No. 101084642. The work of G. K. has been partially supported by project MIS 5154714 of the National Recovery and Resilience Plan Greece 2.0 funded by the European Union under the NextGenerationEU Program.

Disclaimer

This paper was prepared for information purposes and is not a product of HSBC Bank Plc. or its affiliates. Neither HSBC Bank Plc. nor any of its affiliates make any explicit or implied representation or warranty and none of them accept any liability in connection with this paper, including, but not limited to, the completeness, accuracy, reliability of information contained herein and the potential legal, compliance, tax or accounting effects thereof. Copyright HSBC Group 2025.

References

Rajeev Acharya, Dmitry A. Abanin, Laleh Aghababaie-Beni, Igor Aleiner, Trond I. Andersen, Markus Ansmann, Frank Arute, Kunal Arya, Abraham Asfaw, Nikita Astrakhantsev, Juan Atalaya, Ryan Babbush, Dave Bacon, Brian Ballard, Joseph C. Bardin, Johannes Bausch, Andreas Bengtsson, Alexander Bilmes, Sam Blackwell, Sergio Boixo, Gina Bortoli, Alexandre Bourassa, Jenna Bovaird, Leon Brill, Michael Broughton, David A. Browne, Brett Buchea, Bob B. Buckley, David A. Buell, Tim Burger, Brian Burkett, Nicholas Bushnell, Anthony Cabrera, Juan Campero, Hung-Shen Chang, Yu Chen, Zijun Chen, Ben Chiaro, Desmond Chik, Charina Chou, Jahan Claes, Agnetta Y. Cleland, Josh Cogan, Roberto Collins, Paul Conner, William Courtney, Alexander L. Crook, Ben Curtin, Sayan Das, Alex Davies, Laura De Lorenzo, Dripto M. Debroy, Sean Demura, Michel Devoret, Agustin Di Paolo, Paul Donohoe, Ilya Drozdov, Andrew Dunsworth, Clint Earle, Thomas Edlich, Alec Eickbusch, Aviv Moshe Elbag, Mahmoud Elzouka, Catherine Erickson, Lara Faoro, Edward Farhi, Vinicius S. Ferreira, Leslie Flores Burgos, Ebrahim Forati, Austin G. Fowler, Brooks Foxen, Suhas Ganjam, Gonzalo Garcia, Robert Gasca, Elie Genois, William Giang, Craig Gidney, Dar Gilboa, Raja Gosula, Alejandro Grajales Dau, Dietrich Graumann, Alex Greene, Jonathan A. Gross, Steve Habegger, John Hall, Michael C. Hamilton, Monica Hansen, Matthew P. Harrigan, Sean D. Harrington, Francisco J. H. Heras, Stephen Heslin, Paula Heu, Oscar Higgott, Gordon Hill, Jeremy Hilton, George Holland, Sabrina Hong, Hsin-Yuan Huang, Ashley Huff, William J. Huggins, Lev B. Ioffe, Sergei V. Isakov, Justin Iveland, Evan Jeffrey, Zhang Jiang, Cody Jones, Stephen Jordan, Chaitali Joshi, Pavol Juhas, Dvir Kafri, Hui Kang, Amir H. Karamlou, Kostyantyn Kechedzhi, Julian Kelly, Trupti Khaire, Tanuj Khattar, Mostafa Khezri, Seon Kim, Paul V. Klimov, Andrey R. Klots, Bryce Kobrin, Pushmeet Kohli, Alexander N. Korotkov, Fedor Kostritsa, Robin Kothari, Borislav Kozlovskii, John Mark Kreikebaum, Vladislav D. Kurilovich, Nathan Lacroix, David Landhuis, Tiano Lange-Dei, Brandon W. Langley, Pavel Laptev, Kim-Ming Lau, Loïck Le Guevel, Justin Ledford, Joonho Lee, Kenny Lee, Yuri D. Lensky, Shannon Leon, Brian J. Lester, Wing Yan Li, Yin Li, Alexander T. Lill, Wayne Liu, William P. Livingston, Aditya Locharla, Erik Lucero, Daniel Lundahl, Aaron Lunt, Sid Madhuk, Fionn D. Malone, Ashley Maloney, Salvatore Mandrà, James Manyika, Leigh S. Martin, Orion Martin, Steven Martin, Cameron Maxfield, Jarrod R. McClean, Matt McEwen, Seneca Meeks, Anthony Megrant, Xiao Mi, Kevin C. Miao, Amanda Mieszala, Reza Molavi, Sebastian Molina, Shirin Montazeri, Alexis Morvan, Ramis Movassagh, Wojciech Mruczkiewicz, Ofer Naaman, Matthew Neeley, Charles Neill, Ani Nersisyan, Hartmut Neven, Michael Newman, Jiun How Ng, Anthony Nguyen, Murray Nguyen, Chia-Hung Ni, Murphy Yuezhen Niu, Thomas E. O'Brien, William D. Oliver, Alex Opremcak, Kristoffer Ottosson, Andre Petukhov, Alex Pizzuto, John Platt, Rebecca Potter, Orion Pritchard, Leonid P. Pryadko, Chris Quintana, Ganesh Ramachandran, Matthew J. Reagor, John Redding, David M. Rhodes, Gabrielle Roberts, Elliott Rosenberg, Emma Rosenfeld, Pedram Roushan, Nicholas C. Rubin, Negar Saei, Daniel Sank, Kannan Sankaragomathi, Kevin J. Satzinger, Henry F. Schurkus, Christopher Schuster, Andrew W. Senior, Michael J. Shearn, Aaron Shorter, Noah Shutty, Vladimir Shvarts, Shraddha Singh, Volodymyr Sivak, Jindra Skruzny, Spencer Small, Vadim Smelyanskiy, W. Clarke Smith, Rolando D. Somma, Sofia Springer, George Sterling, Doug Strain, Jordan Suchard, Aaron Szasz, Alex Sztein, Douglas Thor, Alfredo Torres, M. Mert Torunbalci, Abeer Vaishnav, Justin Vargas, Sergey Vdovichev, Guifre Vidal, Benjamin Villalonga, Catherine Vollgraff Heidweiller, Steven Waltman, Shannon X. Wang, Brayden Ware, Kate Weber, Travis Weidel, Theodore White, Kristi Wong, Bryan W. K. Woo, Cheng Xing, Z. Jamie Yao, Ping Yeh, Bicheng Ying, Juhwan Yoo, Noureldin Yosri, Grayson Young, Adam Zalcman, Yaxing Zhang, Ningfeng Zhu, Nicholas Zobrist, A. I. Google Quantum, and Collaborators. Quantum error correction below the surface code threshold. *Nature*, 638(8052):920–926, 2025. ISSN 1476-4687. doi: 10.1038/s41586-024-08449-y. URL <https://doi.org/10.1038/s41586-024-08449-y>.

ACM. Acm a.m. turing award honors two researchers who led the development of cornerstone ai technology. 2025. URL <https://awards.acm.org/binaries/content/assets/press-releases/2025/march/turing-award-2024.pdf>. Accessed: 2025-03-05.

T. I. Andersen, N. Astrakhantsev, A. H. Karamlou, J. Berndtsson, J. Motruk, A. Szasz, J. A. Gross, A. Schuckert, T. Westerhout, Y. Zhang, E. Forati, D. Rossi, B. Kobrin, A. Di Paolo, A. R. Klots, I. Drozdov, V. Kurilovich, A. Petukhov, L. B. Ioffe, A. Elben, A. Rath, V. Vitale, B. Vermersch, R. Acharya, L. A. Beni, K. Anderson, M. Ansmann, F. Arute, K. Arya, A. Asfaw, J. Atalaya, B. Ballard, J. C. Bardin, A. Bengtsson, A. Bilmes, G. Bortoli, A. Bourassa, J. Bovaird, L. Brill, M. Broughton, D. A. Browne, B. Buchea, B. B. Buckley, D. A. Buell, T. Burger, B. Burkett,

N. Bushnell, A. Cabrera, J. Campero, H.-S. Chang, Z. Chen, B. Chiaro, J. Claes, A. Y. Cleland, J. Cogan, R. Collins, P. Conner, W. Courtney, A. L. Crook, S. Das, D. M. Debroy, L. De Lorenzo, A. Del Toro Barba, S. Demura, P. Donohoe, A. Dunsworth, C. Earle, A. Eickbusch, A. M. Elbag, M. Elzouka, C. Erickson, L. Faoro, R. Fatemi, V. S. Ferreira, L. Flores Burgos, A. G. Fowler, B. Foxen, S. Ganjam, R. Gasca, W. Giang, C. Gidney, D. Gilboa, M. Giustina, R. Gosula, A. Grajales Dau, D. Graumann, A. Greene, S. Habegger, M. C. Hamilton, M. Hansen, M. P. Harrigan, S. D. Harrington, S. Heslin, P. Heu, G. Hill, M. R. Hoffmann, H.-Y. Huang, T. Huang, A. Huff, W. J. Huggins, S. V. Isakov, E. Jeffrey, Z. Jiang, C. Jones, S. Jordan, C. Joshi, P. Juhas, D. Kafri, H. Kang, K. Kechedzhi, T. Khaire, T. Khattar, M. Khezri, M. Kieferová, S. Kim, A. Kitaev, P. Klimov, A. N. Korotkov, F. Kostritsa, J. M. Kreikebaum, D. Landhuis, B. W. Langley, P. Laptev, K.-M. Lau, L. Le Guevel, J. Ledford, J. Lee, K. W. Lee, Y. D. Lensky, B. J. Lester, W. Y. Li, A. T. Lill, W. Liu, W. P. Livingston, A. Locharla, D. Lundahl, A. Lunt, S. Madhuk, A. Maloney, S. Mandrà, L. S. Martin, O. Martin, S. Martin, C. Maxfield, J. R. McClean, M. McEwen, S. Meeks, K. C. Miao, A. Mieszala, S. Molina, S. Montazeri, A. Morvan, R. Movassagh, C. Neill, A. Nersisyan, M. Newman, A. Nguyen, M. Nguyen, C.-H. Ni, M. Y. Niu, W. D. Oliver, K. Ottosson, A. Pizzuto, R. Potter, O. Pritchard, L. P. Pryadko, C. Quintana, M. J. Reagor, D. M. Rhodes, G. Roberts, C. Rocque, E. Rosenberg, N. C. Rubin, N. Saei, K. Sankaragomathi, K. J. Satzinger, H. F. Schurkus, C. Schuster, M. J. Shearn, A. Shorter, N. Shutty, V. Shvarts, V. Sivak, J. Skrzyn, S. Small, W. Clarke Smith, S. Springer, G. Sterling, J. Suchard, M. Szalay, A. Sztein, D. Thor, A. Torres, M. M. Torunbalci, A. Vaishnav, S. Vdovichev, B. Villalonga, C. Vollgraff Heidweiller, S. Waltman, S. X. Wang, T. White, K. Wong, B. W. K. Woo, C. Xing, Z. Jamie Yao, P. Yeh, B. Ying, J. Yoo, N. Yosri, G. Young, A. Zalcman, N. Zhu, N. Zobrist, H. Neven, R. Babbush, S. Boixo, J. Hilton, E. Lucero, A. Megrant, J. Kelly, Y. Chen, V. Smelyanskiy, G. Vidal, P. Roushan, A. M. Läuchli, D. A. Abanin, and X. Mi. Thermalization and criticality on an analogue-digital quantum simulator. *Nature*, 638(8049):79–85, 2025. ISSN 1476-4687. doi: 10.1038/s41586-024-08460-3. URL <https://doi.org/10.1038/s41586-024-08460-3>.

Frank Arute, Kunal Arya, Ryan Babbush, Dave Bacon, Joseph C. Bardin, Rami Barends, Rupak Biswas, Sergio Boixo, Fernando G. S. L. Brandao, David A. Buell, Brian Burkett, Yu Chen, Zijun Chen, Ben Chiaro, Roberto Collins, William Courtney, Andrew Dunsworth, Edward Farhi, Brooks Foxen, Austin Fowler, Craig Gidney, Marissa Giustina, Rob Graff, Keith Guerin, Steve Habegger, Matthew P. Harrigan, Michael J. Hartmann, Alan Ho, Markus Hoffmann, Trent Huang, Travis S. Humble, Sergei V. Isakov, Evan Jeffrey, Zhang Jiang, Dvir Kafri, Kostyantyn Kechedzhi, Julian Kelly, Paul V. Klimov, Sergey Knysh, Alexander Korotkov, Fedor Kostritsa, David Landhuis, Mike Lindmark, Erik Lucero, Dmitry Lyakh, Salvatore Mandrà, Jarrod R. McClean, Matthew McEwen, Anthony Megrant, Xiao Mi, Kristel Michelsen, Masoud Mohseni, Josh Mutus, Ofer Naaman, Matthew Neeley, Charles Neill, Murphy Yuezen Niu, Eric Ostby, Andre Petukhov, John C. Platt, Chris Quintana, Eleanor G. Rieffel, Pedram Roushan, Nicholas C. Rubin, Daniel Sank, Kevin J. Satzinger, Vadim Smelyanskiy, Kevin J. Sung, Matthew D. Trevithick, Amit Vainsencher, Benjamin Villalonga, Theodore White, Z. Jamie Yao, Ping Yeh, Adam Zalcman, Hartmut Neven, and John M. Martinis. Quantum supremacy using a programmable superconducting processor. *Nature*, 574(7779):505–510, 2019. ISSN 1476-4687. doi: 10.1038/s41586-019-1666-5. URL <https://doi.org/10.1038/s41586-019-1666-5>.

Jacob Biamonte, Peter Wittek, Nicola Pancotti, Patrick Rebentrost, Nathan Wiebe, and Seth Lloyd. Quantum machine learning. *Nature*, 549(7671):195–202, 2017. ISSN 1476-4687. doi: 10.1038/nature23474. URL <https://doi.org/10.1038/nature23474>.

Gilles Brassard, Peter Hoyer, Michele Mosca, and Alain Tapp. Quantum amplitude amplification and estimation. *arXiv preprint quant-ph/0005055*, 2000.

Chen-Hao Chao, Chien Feng, Wei-Fang Sun, Cheng-Kuang Lee, Simon See, and Chun-Yi Lee. Maximum entropy reinforcement learning via energy-based normalizing flow. 2024. URL <https://arxiv.org/abs/2405.13629>.

DeepSeek-AI, Daya Guo, Dejian Yang, Haowei Zhang, Junxiao Song, Ruoyu Zhang, Runxin Xu, Qihao Zhu, Shirong Ma, Peiyi Wang, Xiao Bi, Xiaokang Zhang, Xingkai Yu, Yu Wu, Z. F. Wu, Zhibin Gou, Zhihong Shao, Zhuoshu Li, Ziyi Gao, Aixin Liu, Bing Xue, Bingxuan Wang, Bochao Wu, Bei Feng, Chengda Lu, Chenggang Zhao, Chengqi Deng, Chenyu Zhang, Chong Ruan, Damai Dai, Deli Chen, Dongjie Ji, Erhang Li, Fangyun Lin, Fucong Dai, Fuli Luo, Guangbo Hao, Guanting Chen, Guowei Li, H. Zhang, Han Bao, Hanwei Xu, Haocheng Wang, Honghui Ding,

Huajian Xin, Huazuo Gao, Hui Qu, Hui Li, Jianzhong Guo, Jiashi Li, Jiawei Wang, Jingchang Chen, Jingyang Yuan, Junjie Qiu, Junlong Li, J. L. Cai, Jiaqi Ni, Jian Liang, Jin Chen, Kai Dong, Kai Hu, Kaige Gao, Kang Guan, Kexin Huang, Kuai Yu, Lean Wang, Lecong Zhang, Liang Zhao, Litong Wang, Liyue Zhang, Lei Xu, Leyi Xia, Mingchuan Zhang, Minghua Zhang, Minghui Tang, Meng Li, Miaojun Wang, Mingming Li, Ning Tian, Panpan Huang, Peng Zhang, Qiancheng Wang, Qinyu Chen, Qiushi Du, Ruiqi Ge, Ruisong Zhang, Ruizhe Pan, Runji Wang, R. J. Chen, R. L. Jin, Ruyi Chen, Shanghao Lu, Shangyan Zhou, Shanhua Chen, Shengfeng Ye, Shiyu Wang, Shuiping Yu, Shunfeng Zhou, Shuting Pan, S. S. Li, Shuang Zhou, Shaoqing Wu, Shengfeng Ye, Tao Yun, Tian Pei, Tianyu Sun, T. Wang, Wangding Zeng, Wanja Zhao, Wen Liu, Wenfeng Liang, Wenjun Gao, Wenqin Yu, Wentao Zhang, W. L. Xiao, Wei An, Xiaodong Liu, Xiaohan Wang, Xiaokang Chen, Xiaotao Nie, Xin Cheng, Xin Liu, Xin Xie, Xingchao Liu, Xinyu Yang, Xinyuan Li, Xuecheng Su, Xuheng Lin, X. Q. Li, Xiangyue Jin, Xiaojin Shen, Xiaosha Chen, Xiaowen Sun, Xiaoxiang Wang, Xinnan Song, Xinyi Zhou, Xianzu Wang, Xinxia Shan, Y. K. Li, Y. Q. Wang, Y. X. Wei, Yang Zhang, Yanhong Xu, Yao Li, Yao Zhao, Yaofeng Sun, Yaohui Wang, Yi Yu, Yichao Zhang, Yifan Shi, Yiliang Xiong, Ying He, Yishi Piao, Yisong Wang, Yixuan Tan, Yiyang Ma, Yiyuan Liu, Yongqiang Guo, Yuan Ou, Yuduan Wang, Yue Gong, Yuheng Zou, Yujia He, Yunfan Xiong, Yuxiang Luo, Yuxiang You, Yuxuan Liu, Yuyang Zhou, Y. X. Zhu, Yanhong Xu, Yanping Huang, Yaohui Li, Yi Zheng, Yuchen Zhu, Yunxian Ma, Ying Tang, Yukun Zha, Yuting Yan, Z. Z. Ren, Zehui Ren, Zhangli Sha, Zhe Fu, Zhean Xu, Zhenda Xie, Zhengyan Zhang, Zhewen Hao, Zhicheng Ma, Zhigang Yan, Zhiyu Wu, Zihui Gu, Zijia Zhu, Zijun Liu, Zilin Li, Ziwei Xie, Ziyang Song, Zizheng Pan, Zhen Huang, Zhipeng Xu, Zhongyu Zhang, and Zhen Zhang. Deepseek-r1: Incentivizing reasoning capability in llms via reinforcement learning. 2025a. URL <https://arxiv.org/abs/2501.12948>.

DeepSeek-AI, Aixin Liu, Bei Feng, Bing Xue, Bingxuan Wang, Bochao Wu, Chengda Lu, Chenggang Zhao, Chengqi Deng, Chenyu Zhang, Chong Ruan, Damai Dai, Daya Guo, Dejian Yang, Deli Chen, Dongjie Ji, Erhang Li, Fangyun Lin, Fucong Dai, Fuli Luo, Guangbo Hao, Guanting Chen, Guowei Li, H. Zhang, Han Bao, Hanwei Xu, Haocheng Wang, Haowei Zhang, Honghui Ding, Huajian Xin, Huazuo Gao, Hui Li, Hui Qu, J. L. Cai, Jian Liang, Jianzhong Guo, Jiaqi Ni, Jiashi Li, Jiawei Wang, Jin Chen, Jingchang Chen, Jingyang Yuan, Junjie Qiu, Junlong Li, Junxiao Song, Kai Dong, Kai Hu, Kaige Gao, Kang Guan, Kexin Huang, Kuai Yu, Lean Wang, Lecong Zhang, Lei Xu, Leyi Xia, Liang Zhao, Litong Wang, Liyue Zhang, Meng Li, Miaojun Wang, Mingchuan Zhang, Minghua Zhang, Minghui Tang, Mingming Li, Ning Tian, Panpan Huang, Peiyi Wang, Peng Zhang, Qiancheng Wang, Qihao Zhu, Qinyu Chen, Qiushi Du, R. J. Chen, R. L. Jin, Ruiqi Ge, Ruisong Zhang, Ruizhe Pan, Runji Wang, Runxin Xu, Ruoyu Zhang, Ruyi Chen, S. S. Li, Shanghao Lu, Shangyan Zhou, Shanhua Chen, Shaoqing Wu, Shengfeng Ye, Shengfeng Ye, Shirong Ma, Shiyu Wang, Shuang Zhou, Shuiping Yu, Shunfeng Zhou, Shuting Pan, T. Wang, Tao Yun, Tian Pei, Tianyu Sun, W. L. Xiao, Wangding Zeng, Wanja Zhao, Wei An, Wen Liu, Wenfeng Liang, Wenjun Gao, Wenqin Yu, Wentao Zhang, X. Q. Li, Xiangyue Jin, Xianzu Wang, Xiao Bi, Xiaodong Liu, Xiaohan Wang, Xiaojin Shen, Xiaokang Chen, Xiaokang Zhang, Xiaosha Chen, Xiaotao Nie, Xiaowen Sun, Xiaoxiang Wang, Xin Cheng, Xin Liu, Xin Xie, Xingchao Liu, Xingkai Yu, Xinnan Song, Xinxia Shan, Xinyi Zhou, Xinyu Yang, Xinyuan Li, Xuecheng Su, Xuheng Lin, Y. K. Li, Y. Q. Wang, Y. X. Wei, Y. X. Zhu, Yang Zhang, Yanhong Xu, Yanhong Xu, Yanping Huang, Yao Li, Yao Zhao, Yaofeng Sun, Yaohui Li, Yaohui Wang, Yi Yu, Yi Zheng, Yichao Zhang, Yifan Shi, Yiliang Xiong, Ying He, Ying Tang, Yishi Piao, Yisong Wang, Yixuan Tan, Yiyang Ma, Yiyuan Liu, Yongqiang Guo, Yu Wu, Yuan Ou, Yuchen Zhu, Yuduan Wang, Yue Gong, Yuheng Zou, Yujia He, Yukun Zha, Yunfan Xiong, Yunxian Ma, Yuting Yan, Yuxiang Luo, Yuxiang You, Yuxuan Liu, Yuyang Zhou, Z. F. Wu, Z. Z. Ren, Zehui Ren, Zhangli Sha, Zhe Fu, Zhean Xu, Zhen Huang, Zhen Zhang, Zhenda Xie, Zhengyan Zhang, Zhewen Hao, Zhibin Gou, Zhicheng Ma, Zhigang Yan, Zihong Shao, Zhipeng Xu, Zhiyu Wu, Zhongyu Zhang, Zhuoshu Li, Zihui Gu, Zijia Zhu, Zijun Liu, Zilin Li, Ziwei Xie, Ziyang Song, Ziyi Gao, and Zizheng Pan. Deepseek-v3 technical report. 2025b. URL <https://arxiv.org/abs/2412.19437>.

Daoyi Dong, Chunlin Chen, Hanxiong Li, and Tzyh-Jong Tarn. Quantum reinforcement learning. *IEEE Transactions on Systems, Man, and Cybernetics, Part B (Cybernetics)*, 38(5):1207–1220, 2008.

Vedran Dunjko, Jacob M Taylor, and Hans J Briegel. Advances in quantum reinforcement learning. In *2017 IEEE international conference on systems, man, and cybernetics (SMC)*, pages 282–287. IEEE, 2017.

Dongxin Gao, Daojin Fan, Chen Zha, Jiahao Bei, Guoqing Cai, Jianbin Cai, Sirui Cao, Fusheng Chen, Jiang Chen, Kefu Chen, Xiwei Chen, Xiqing Chen, Zhe Chen, Zhiyuan Chen, Zihua Chen, Wenhao Chu, Hui Deng, Zhibin Deng, Pei Ding, Xun Ding, Zhuzhengqi Ding, Shuai Dong, Yupeng Dong, Bo Fan, Yuanhao Fu, Song Gao, Lei Ge, Ming Gong, Jiacheng Gui, Cheng Guo, Shaojun Guo, Xiaoyang Guo, Lianchen Han, Tan He, Linyin Hong, Yisen Hu, He-Liang Huang, Yong-Heng Huo, Tao Jiang, Zuokai Jiang, Honghong Jin, Yunxiang Leng, Dayu Li, Dongdong Li, Fangyu Li, Jiaqi Li, Jinjin Li, Junyan Li, Junyun Li, Na Li, Shaowei Li, Wei Li, Yuhuai Li, Yuan Li, Futian Liang, Xuelian Liang, Nanxing Liao, Jin Lin, Weiping Lin, Dailin Liu, Hongxiu Liu, Maliang Liu, Xinyu Liu, Xuemeng Liu, Yancheng Liu, Haoxin Lou, Yuwei Ma, Lingxin Meng, Hao Mou, Kailiang Nan, Binghan Nie, Meijuan Nie, Jie Ning, Le Niu, Wenyi Peng, Haoran Qian, Hao Rong, Tao Rong, Huiyan Shen, Qiong Shen, Hong Su, Feifan Su, Chenyin Sun, Liangchao Sun, Tianzuo Sun, Yingxiu Sun, Yimeng Tan, Jun Tan, Longyue Tang, Wenbing Tu, Cai Wan, Jiafei Wang, Biao Wang, Chang Wang, Chen Wang, Chu Wang, Jian Wang, Liangyuan Wang, Rui Wang, Shengtao Wang, Xiaomin Wang, Xinzhe Wang, Xunxun Wang, Yeru Wang, Zuolin Wei, Jiazhou Wei, Dachao Wu, Gang Wu, Jin Wu, Shengjie Wu, Yulin Wu, Shiyong Xie, Lianjie Xin, Yu Xu, Chun Xue, Kai Yan, Weifeng Yang, Xinpeng Yang, Yang Yang, Yangsen Ye, Zhenping Ye, Chong Ying, Jiale Yu, Qinjing Yu, Wenhui Yu, Xiangdong Zeng, Shaoyu Zhan, Feifei Zhang, Haibin Zhang, Kaili Zhang, Pan Zhang, Wen Zhang, Yiming Zhang, Yongzhuo Zhang, Lixiang Zhang, Guming Zhao, Peng Zhao, Xianhe Zhao, Xintao Zhao, Youwei Zhao, Zhong Zhao, Luyuan Zheng, Fei Zhou, Liang Zhou, Na Zhou, Naibin Zhou, Shifeng Zhou, Shuang Zhou, Zhengxiao Zhou, Chengjun Zhu, Qingling Zhu, Guihong Zou, Haonan Zou, Qiang Zhang, Chao-Yang Lu, Cheng-Zhi Peng, Xiaobo Zhu, and Jian-Wei Pan. Establishing a new benchmark in quantum computational advantage with 105-qubit zuchongzhi 3.0 processor. *PRL*, 134(9):090601, March 2025. doi: 10.1103/PhysRevLett.134.090601. URL <https://link.aps.org/doi/10.1103/PhysRevLett.134.090601>.

Google Quantum AI. Choosing hardware for your qsim simulation. https://quantumai.google/qsim/choose_hw, 2025. Accessed 15 May 2025.

Tuomas Haarnoja, Aurick Zhou, Pieter Abbeel, and Sergey Levine. Soft actor-critic: Off-policy maximum entropy deep reinforcement learning with a stochastic actor. 2018. URL <https://arxiv.org/abs/1801.01290>.

Aram W. Harrow, Avinatan Hassidim, and Seth Lloyd. Quantum algorithm for linear systems of equations. *PRL*, 103(15):150502, October 2009. doi: 10.1103/PhysRevLett.103.150502. URL <https://link.aps.org/doi/10.1103/PhysRevLett.103.150502>.

Cupjin Huang, Fang Zhang, Michael Newman, Xiaotong Ni, Dawei Ding, Junjie Cai, Xun Gao, Tenghui Wang, Feng Wu, Gengyan Zhang, Hsiang-Sheng Ku, Zhengxiong Tian, Junyin Wu, Haihong Xu, Huanjun Yu, Bo Yuan, Mario Szegedy, Yaoyun Shi, Hui-Hai Zhao, Chunqing Deng, and Jianxin Chen. Efficient parallelization of tensor network contraction for simulating quantum computation. *Nature Computational Science*, 1(9):578–587, 2021. ISSN 2662-8457. doi: 10.1038/s43588-021-00119-7. URL <https://doi.org/10.1038/s43588-021-00119-7>.

Hsin-Yuan Huang, Michael Broughton, Jordan Cotler, Sitan Chen, Jerry Li, Masoud Mohseni, Hartmut Neven, Ryan Babbush, Richard Kueng, John Preskill, and Jarrod R. McClean. Quantum advantage in learning from experiments. *Science*, 376(6598):1182–1186, June 2022. doi: 10.1126/science.abn7293. URL <https://doi.org/10.1126/science.abn7293>.

Sofiene Jerbi, Lea M Trenkwalder, Hendrik Poulsen Nautrup, Hans J Briegel, and Vedran Dunjko. Quantum enhancements for deep reinforcement learning in large spaces. *PRX Quantum*, 2(1):010328, 2021.

Yu-Xin Jin, Zi-Wei Wang, Hong-Ze Xu, Wei-Feng Zhuang, Meng-Jun Hu, and Dong E. Liu. Ppo-q: Proximal policy optimization with parametrized quantum policies or values. 2025. URL <https://arxiv.org/abs/2501.07085>.

Timothy P. Lillicrap, Jonathan J. Hunt, Alexander Pritzel, Nicolas Heess, Tom Erez, Yuval Tassa, David Silver, and Daan Wierstra. Continuous control with deep reinforcement learning. 2019. URL <https://arxiv.org/abs/1509.02971>.

Yong Liu, Yaojian Chen, Chu Guo, Jiawei Song, Xinmin Shi, Lin Gan, Wenzhao Wu, Wei Wu, Haohuan Fu, Xin Liu, Dexun Chen, Zhifeng Zhao, Guangwen Yang, and Jiangang Gao. Verifying quantum advantage experiments with multiple amplitude tensor network contraction. *PRL*, 132(3):030601, January 2024. doi: 10.1103/PhysRevLett.132.030601. URL <https://link.aps.org/doi/10.1103/PhysRevLett.132.030601>.

Kin Ian Lo, Mehrnoosh Sadrzadeh, and Shane Mansfield. Generalised winograd schema and its contextuality. *Electronic Proceedings in Theoretical Computer Science*, 384:187–202, August 2023. ISSN 2075-2180. doi: 10.4204/eptcs.384.11. URL <http://dx.doi.org/10.4204/eptcs.384.11>.

NVIDIA. Nvidia cuda-q. <https://developer.nvidia.com/cuda-q/>, 2022.

NVIDIA. Accelerate generalist humanoid robot development with nvidia isaac gr0ot n1, 2025. URL <https://developer.nvidia.com/blog/accelerate-generalist-humanoid-robot-development-with-nvidia-isaac-gr0ot-n1/>. Accessed: 2025-05-13.

Giuseppe Davide Paparo, Vedran Dunjko, Adi Makmal, Miguel Angel Martin-Delgado, and Hans J Briegel. Quantum speedup for active learning agents. *Physical Review X*, 4(3):031002, 2014.

Antonin Raffin. RL baselines3 zoo. <https://github.com/DLR-RM/rl-baselines3-zoo>, 2020.

Kylie Robison. Openai cofounder ilya sutskever says the way ai is built is about to change, 12 2024. URL <https://www.theverge.com/2024/12/13/24320811/what-ilya-sutskever-sees-openai-model-data-training>.

Siddharth Samsi, Dan Zhao, Joseph McDonald, Baolin Li, Adam Michaleas, Michael Jones, William Bergeron, Jeremy Kepner, Devesh Tiwari, and Vijay Gadepally. From words to watts: Benchmarking the energy costs of large language model inference. 2023. URL <https://arxiv.org/abs/2310.03003>.

John Schulman, Filip Wolski, Prafulla Dhariwal, Alec Radford, and Oleg Klimov. Proximal policy optimization algorithms. 2017. URL <https://arxiv.org/abs/1707.06347>.

Mark Towers, Ariel Kwiatkowski, Jordan Terry, John U Balis, Gianluca De Cola, Tristan Deleu, Manuel Goulão, Andreas Kallinteris, Markus Krimmel, Arjun KG, et al. Gymnasium: A standard interface for reinforcement learning environments. *arXiv preprint arXiv:2407.17032*, 2024.

Ashish Vaswani, Noam Shazeer, Niki Parmar, Jakob Uszkoreit, Llion Jones, Aidan N. Gomez, Łukasz Kaiser, and Illia Polosukhin. Attention is all you need. 2023. URL <https://arxiv.org/abs/1706.03762>.

Yunfei Wang and Junyu Liu. A comprehensive review of quantum machine learning: from nisq to fault tolerance. *Reports on Progress in Physics*, 87(11):116402, 2024. ISSN 0034-4885. doi: 10.1088/1361-6633/ad7f69. URL <https://dx.doi.org/10.1088/1361-6633/ad7f69>.

Sarah Wells. Generative ai's energy problem today is foundational. <https://spectrum.ieee.org/license-to-spill>, 2025. Accessed 15 May 2025.

Shaojun Wu, Shan Jin, Dingding Wen, Donghong Han, and Xiaoting Wang. Quantum reinforcement learning in continuous action space. *Quantum*, 9:1660, 2025.

Adam Yanxiao Zhao. Humanoid v4 sac continuous action seed5, 12 2023a. URL https://huggingface.co/sdpkjc/Humanoid-v4-sac_continuous_action-seed5.

Adam Yanxiao Zhao. Humanoid v4 td3 continuous action seed3, 12 2023b. URL https://huggingface.co/sdpkjc/Humanoid-v4-td3_continuous_action-seed3.

Adam Yanxiao Zhao. Humanoid v4 ppo fix continuous action seed4, 1 2024. URL https://huggingface.co/sdpkjc/Humanoid-v4-ppo_fix_continuous_action-seed4.

A Appendix

A.1 Limitations

A.1.1 Training hDQNN with qtDNN surrogate

The assumption that a quantum tangential deep neural network (qtDNN) can be trained as a good approximation to a given QL could only be reasonable for each mini-batch of training data (see Fig. 6) in off-policy reinforcement learning frameworks. It is because the sampled distribution of a general PQC is exponentially hard to simulate with classical computing resources Arute et al. [2019], Acharya et al. [2025].

Moreover, during the experiment, we implemented qtDNN as a 3-layer MLP and observed that training is most efficient when the hidden layer has $L_h = 2^{N+1}$ neurons for a N -qubit wide PQC. As N -qubit spans a Hilbert space $\mathcal{H}_{Nq} \cong \mathbb{C}^{2^N} \cong \mathbb{R}^{2^{N+1}}$, the experimentally observed best hidden layer's linear space $\mathcal{L}_h \cong \mathbb{R}^{2^{N+1}} \cong \mathcal{H}_{Nq}$ for $N = 10$ in the experiment achieving a high score. Reducing the hidden linear space \mathcal{L}_h to \mathbb{R}^{2^N} has been observed to drastically reduce model performance in the final score. The observations indicate that physics-inspired appropriate multi-qubit state representation by the hidden layer is critical. Therefore, it is reasonable to expect, the number of neurons required for 3-layer MLP qtDNN scales according to 2^{N+1} with N qubits in the PQC it approximates locally. We also note that the optimal 3-layer MLP design of qtDNN seems to be unexpectedly independent of PQC depth, M . This exponential resource scaling would limit the 3-layer MLP implementation of qtDNN to relatively narrow (in qubit count) PQC. The limitation on PQC width could further limit the ability for hDQNN + qtDNN to learn complex AI/ML tasks involving a vast number of correlated degrees of freedoms and hinder its applications in the Large Language Models (LLMs) DeepSeek-AI et al. [2025a,b] and advanced robotic controls in unpredictable real-world interactive conditions as in NVIDIA [2025]. Future development of novel qtDNN architecture might significantly improve the scaling efficiency by tailoring the qtDNN design to respect the structure of a given PQC and bound its resource requirements with a function of N_b . For example, tensor network methods could approximate a PQC with a given structure efficiently Liu et al. [2024], Huang et al. [2021]. However, even with the potentially large resource requirements scaling exponentially with the number of qubits involved in sampling, we could argue that this limitation is only present in training and the inference data flow of a trained hDQNN is potentially exponentially more efficient as forward pass through the PQC could be carried out on physical QPUs.

For the inference, physical QPUs could carry out PQC operations directly on all qubits without the requirement of exponentially scaling physical computing resources Acharya et al. [2025]. Moreover, the superconducting QPU's 10s ns level quantum entangling gate times Gao et al. [2025] are preferred for co-processing with classical neural networks because the gap in clock rates is much smaller as compared to trapped ion and neutral atom platforms' average entangling gate times around 0.5 ms. Here, we note that even for SOTA high-connectivity superconducting quantum processors, each PQC call with $S = 1,000$ will take about $t_{qc} \sim M \times 50 \text{ ns} + 100 \text{ ns} \sim 0.6 \mu\text{s}$ (assuming a single-qubit and a two-qubit gates in sequence take 50 ns and measurement take 100 ns), leading to a per PQC Call to backend with $S = 1,000$ shots consuming $S \times t_{qc} \sim 0.6 \text{ ms}$ in inference step. Therefore, having fast gates is practically useful for quantum reinforcement learning tasks.

In terms of applying this hDQNN+qtDNN method to a variety of different RL environments, only Humanoid-v4 and the simple Pendulum-v1 were attempted due to time and resource limitations. Even though they represent two extremes of complexities in Gymnasium continuous variable reinforcement learning benchmarks and achieved good results, the long PQC simulation time became a bottleneck making it challenging to extend the experimentation to other environments within the short time available to prepare the paper. However, it is straightforward to apply hDQNN + qtDNN for enhancing reinforcement learning in other useful scenarios involving both continuous and discrete observation and action spaces. Integration with the trailblazing AI models' training and inference pipelines DeepSeek-AI et al. [2025a] could be among the topics in future researches.

In the end, hDQNN requires PQC to be executed on a physical or simulated QPU. Real-world QPUs in the near-term have noises (errors) in quantum operations they carry out. Therefore, in this work, we tested the noise tolerance of hDQNN + qtDNN method in learning Humanoid-v4. The hDQNN + qtDNN model having PQC bit-flip and phase-flip error rates of 10^{-3} performs on par and even potentially better than classical SOTA models in terms of rewards they achieved given a

similar compute. However, a larger 10^{-2} error rate in physical quantum gates would lead to a final reward lower than SOTA models. On the other hand, we further noticed hDQNN + qtDNN model demonstrated faster learning with elevated error rates in quantum gates and attribute this to quantum gate noises (errors) having the same effect of larger exploration noises in classical SOTA models. We note that hyper parameters are kept the same between comparable alternative quantum and classical models presented in the main text. We further note that, as we took the most probable bitstring from sampling PQC over S identical shots as the output \mathbf{q}_o of a QL in hDQNN for a given input, \mathbf{q}_i , reducing the number of shots S , in each sampling for estimating \mathbf{q}_o would increase the noises in \mathbf{q}_o . This increased sampling noise impacts the results in a similar way as errors in quantum operations.

A.1.2 The inefficiency of training hDQNN without qtDNN surrogate

Because $I \times O$ different circuits are required to estimate all the gradients of a QL with I input dimensions and O output dimensions and each circuit needs a number, S , of shots to have the statistics for estimating the observables used to calculate gradients. Moreover, learning for complex problems with a high sample data efficiency would require training data to be sampled from past experiences in mini-batches of size N_b for each DNN update with batch optimization as in Haarnoja et al. [2018]. Therefore, existing QML methods that directly estimate gradients of the QL are faced with a prohibitive practical training overhead proportional to $I \times O \times S \times N_b$ for running on real QPU that can only run one shot at a time. For example, in the case of using a fast superconducting Josephson junction quantum processor that has gate time as short as 20 ns and measurement time in the range of 100 ns as seen in Acharya et al. [2025], Gao et al. [2025], a 10-layer 10-qubit PQC (QL) would need $I = 220$ and $O = 10$ with $N_b = 256$ and $S = 1000$ in our example for learning complex Humanoid-v4 environment. In this case, each update to model DNN parameters would require about 281.6 s. Considering that typical classical RL training even for simple tasks would likely require $\sim 10^6$ update steps similar to Haarnoja et al. [2018], this would translate to more than 10 years of training.

A.2 Proof of Theorem 1 on the Local gradient fidelity of qtDNN

Proof. Let $\mathcal{B} \subset \mathbb{R}^d$ be the mini-batch, contained in the closed ball $\overline{B}_r(\bar{x})$. Because Q is C^1 on an open neighbourhood of $\overline{B}_r(\bar{x})$, its Jacobian J_Q is Lipschitz-continuous: we can fix a constant $L > 0$ such that $\|J_Q(x) - J_Q(y)\| \leq L\|x - y\|$ for all $x, y \in \overline{B}_r(\bar{x})$. Set $M = \|\nabla^2 Q(\bar{x})\|$ and $\delta = \max(\varepsilon_1, \varepsilon_2) - \frac{1}{2}Lr^2 > 0$.

Step 1. Approximating the affine Taylor part. Write $h = x - \bar{x}$. First-order Taylor expansion gives $Q(x) = Q(\bar{x}) + J_Q(\bar{x})h + \rho(x)$, where the remainder satisfies the integral form

$$\rho(x) = \int_0^1 [J_Q(\bar{x} + th) - J_Q(\bar{x})]h dt. \quad (1)$$

Define the affine map $P(x) := Q(\bar{x}) + J_Q(\bar{x})h$. The universal-approximation theorem ensures that there exists an MLP Q_θ such that

$$\max_{x \in \mathcal{B}} \|Q_\theta(x) - P(x)\| \leq \delta, \quad \max_{x \in \mathcal{B}} \|\nabla Q_\theta(x) - J_Q(\bar{x})\| \leq \delta. \quad (2)$$

Step 2. Bounding the remainder ρ and its gradient. Because J_Q is L -Lipschitz and $\|h\| \leq r$, from (1) we obtain

$$\|\rho(x)\| \leq \int_0^1 L t \|h\|^2 dt = \frac{1}{2}L\|h\|^2 \leq \frac{1}{2}Lr^2. \quad (3)$$

Differentiating (1) with respect to x yields, using $\nabla_x h = I$,

$$\nabla \rho(x) = \int_0^1 t \nabla^2 Q(\bar{x} + th) h dt.$$

Hence

$$\|\nabla \rho(x)\| \leq \int_0^1 t \|\nabla^2 Q(\bar{x} + th)\| \|h\| dt \leq \frac{1}{2}(M + Lr)r. \quad (4)$$

Step 3. Uniform error bounds on \mathcal{B} . For any $x \in \mathcal{B}$, combine (2) with (3):

$$\|Q_\theta(x) - Q(x)\| \leq \underbrace{\|Q_\theta(x) - P(x)\|}_{\leq \delta} + \underbrace{\|\rho(x)\|}_{\leq \frac{1}{2}Lr^2} \leq \delta + \frac{1}{2}Lr^2 = \varepsilon_1.$$

Likewise, using (2) and (4),

$$\|\nabla Q_\theta(x) - \nabla Q(x)\| \leq \underbrace{\|\nabla Q_\theta(x) - J_Q(\bar{x})\|}_{\leq \delta} + \underbrace{\|\nabla \rho(x)\|}_{\leq \frac{1}{2}(M+Lr)r} \leq \delta + \frac{1}{2}(M+Lr)r = \varepsilon_2.$$

Step 4. Impact on back-propagation. Inside the computation graph, replacing Q by Q_θ changes the per-sample loss by at most ε_1 , and perturbs every mini-batch gradient entering the upstream network by at most ε_2 . Thus all parameter updates incur an additive $\mathcal{O}(\max(\varepsilon_1, \varepsilon_2))$ error, completing the proof. \square

B Mathematical formalization of the hDQNN-TD3’s components

The parameterized quantum circuit (PQC) in the hDQNN-TD3 is a variational circuit designed for NISQ devices, utilizing N qubits to act as a quantum hidden layer within the actor network, taking its inputs from the DNN’s previous layer’s extracted features. It consists of M layers, each comprising single-qubit rotation gates and entangling CZ gates.

Formally, the PQC transforms an input vector \mathbf{q}_i into a probability distribution over bitstrings \mathbf{q}_o by the following:

$$|\psi(\mathbf{q}_i)\rangle = U(\mathbf{q}_i)|0\rangle^{\otimes N} \quad (2)$$

Where U is a sequence of parameterised quantum gates acting on the N qubits. (initially in the $|0\rangle^{\otimes N}$ states):

$$U(\mathbf{q}_i) = \prod_{l=1}^M \left[\prod_{i,j \in \{1, \dots, N\}} R(\theta_{i,l}, \phi_{i,l}) O_{\{i,j,l\}} \right] \quad (3)$$

Here, $R(\theta_{i,l}, \phi_{i,l})$ is a single-qubit rotation gate around the X -axis and Z -axis on qubit i in layer l by $\theta_{i,l}$ and $\phi_{i,l}$ degrees respectively.

Additionally, $O_{\{i,j,l\}}$ represents an entangling operator acting on the qubits i and j in the l layer when $i \neq j$. When $i = j$ we define $O_{\{i,j,l\}} = \mathbb{I}$ as an identity operator. For instance, we can pose $O_{\{i,j,l\}} = \text{CNOT}_{i,j,l}$ which is a controlled-NOT gate between qubits i and j . In the hDQNN-TD3, $O_{\{i,j,l\}} = \text{CZ}_{i,j,l}$.

Altogether, these gates constitute the unitary $U(\mathbf{q}_i)$, which acts on the N -qubit initial state $|0\rangle^{\otimes N}$ (or a suitably encoded feature state) to produce the output state $|\psi(\mathbf{q}_i)\rangle$.

When measuring the qubits in the computational basis, one obtains a bitstring $\mathbf{q}_o \in \{0, 1\}^N$, with probability:

$$P(\mathbf{q}_o | \mathbf{q}_i) = |\langle \mathbf{q}_o | \psi(\mathbf{q}_i) \rangle|^2 \quad (4)$$

B.1 Equations for the qtDNN surrogate

Problem statement. During each *forward* pass the real PQC (or its CUDA-Q simulation) is executed to generate a bit-string $\mathbf{q}_o \in \{0, 1\}^N$; the qtDNN is invoked *only in the backward pass* as a differentiable proxy that supplies $\nabla_\theta \hat{p}$ without additional quantum evaluations. To this end we draw minibatches of pairs $(\mathbf{q}_i, \mathbf{q}_o)$ where $\mathbf{q}_i \in \mathbb{R}^{2NM} \otimes \mathbb{N}^{2M}$ are the rotation angles and pairs of qubit

indices fed to the PQC and $\mathbf{q}_o \in \{0, 1\}^N$ is a bit-string obtained from measurements over multiple shots of executing the same quantum circuit. In hDQNN-TD3, the bit-string is taken as the most probable string among the bit-strings obtained from multiple shots. The qtDNN learns a mapping

$$f_{\text{qtDNN}} : \mathbf{q}_i, \omega \longmapsto \hat{\mathbf{p}} = (\hat{p}_{\omega,1}, \dots, \hat{p}_{\omega,N}), \quad \hat{p}_{\omega,k} \in (0, 1), \quad (5)$$

where ω denotes the qtDNN parameters and $\hat{p}_{\omega,k}$ is the surrogate's estimate of the marginal probability that qubit k is measured in state $|1\rangle$.

Training objective. Ideally one would minimise the cross-entropy with respect to the *joint* distribution produced by the PQC, $P_{\text{PQC}}(\mathbf{q}_o \mid \theta)$, namely $\mathcal{L} = -\log P_{\text{PQC}}(\mathbf{q}_o \mid \theta)$. However estimating that joint requires $\Omega(2^N)$ shots per input and is infeasible even for the moderate $N = 10$ qubits used in our study. Following prior work on quantum-model surrogates, we therefore adopt the factorised *binary cross-entropy* (BCE)

$$\mathcal{L}_{\text{qtDNN}}(\omega) = - \sum_{k=1}^N \left[\mathbf{q}_{o,k} \log \hat{p}_{\omega,k} + (1 - \mathbf{q}_{o,k}) \log(1 - \hat{p}_{\omega,k}) \right], \quad (6)$$

$$= \mathbb{E}_{(\theta, \mathbf{q}_o) \sim \mathcal{M}} [\text{BCE}(\mathbf{q}_o, f_{\text{qtDNN}}(\mathbf{q}_i; \omega))], \quad (7)$$

where \mathcal{M} is the minibatch of replay buffer of observed $(\mathbf{q}_i, \mathbf{q}_o)$ pairs.

Independence assumption. Equation (6) treats qubits as independent Bernoulli variables, whereas the true PQC may entangle them. We demonstrated theoretically that this approximation is adequate for gradient propagation. Moreover, the stability of the learning process shows that the surrogate successfully reproduces the expectation values of the PQC. Future work could replace the factorised model with an autoregressive density estimator to capture higher-order correlations without the exponential shot overhead.

B.2 Forward pass of the hDQNN (inference, no RL)

The hybrid actor is evaluated in three deterministic stages; no reinforcement-learning logic or qtDNN surrogate is involved in this pure inference path.

1. PreDNN → rotation angles. Given an observation $\mathbf{x} \in \mathbb{R}^n$, the PreDNN (a feed-forward MLP) produces a latent vector $\mathbf{z}_{\text{pre}} \in \mathbb{R}^{(2N+2)M+d_{\text{c-link}}}$, where the last $d_{\text{c-link}}$ elements are passed to PostDNN directly. The rest of the elements are rescaled to $[-\pi, \pi]^{2NM}$ or rounded to integers \mathbb{N}^{2M} as follows. The rescaled part is split into the pair of rotation angles for every qubit in every layer of the PQC,

$$\begin{aligned} \theta &= \mathbf{z}_{\text{pre}}^{1:N \times M}, & \phi &= \mathbf{z}_{\text{pre}}^{N \times M+1:2N \times M}, & \mathbf{k} &= \mathbf{z}_{\text{pre}}^{2N \times M+1:(2N+2)M}, \\ \mathbf{q}_i &= (\theta, \phi, \mathbf{k}) \in [-\pi, \pi]^{2N \times M} \otimes \mathbb{N}^{2M}. \end{aligned} \quad (8)$$

2. PQC → expectation values. The rotation-encoded angles drive the parameterised quantum circuit $U(\mathbf{q}_i)$, producing the state $|\psi(\mathbf{q}_i)\rangle$. Instead of sampling a bit-string, the implementation measures the *Pauli-Z* expectation of each qubit,

$$z_k^{(q)} = \langle \psi(\mathbf{q}_i) | Z_k | \psi(\mathbf{q}_i) \rangle, \quad k = 1, \dots, N, \quad (9)$$

yielding the vector $\mathbf{z}_q = (z_1^{(q)}, \dots, z_N^{(q)}) \in -1, 1^N$. A single bit-string sample is drawn only for logging purposes.

3. PostDNN → action prediction. An optional “skip” connection concatenates the last $d_{\text{c-link}} \leq N$ entries of \mathbf{z}_{pre} , $\mathbf{z}_{\text{c-link}}$, to the quantum layer output bit-string:

$$\tilde{\mathbf{z}} = [\mathbf{z}_q \parallel \mathbf{z}_{\text{c-link}}].$$

The resulting feature vector $\tilde{\mathbf{z}}$ is fed to PostDNN, producing the final continuous action

$$\mathbf{y}_{\text{pred}} = f_{\text{PostDNN}}(\tilde{\mathbf{z}}) \in \mathbb{R}^{n_a}. \quad (10)$$

Summary. Putting the three stages together, the deterministic forward map of the actor is

$$\boxed{\mathbf{x} \xrightarrow{f_{\text{PreDNN}}} \mathbf{z}_{\text{pre}} \xrightarrow{\text{PQC}} \mathbf{z}_{\text{q}} \xrightarrow{f_{\text{PostDNN}}} \mathbf{y}_{\text{pred}}}.$$

All quantum layer's bit-strings are computed by the CUDA-Q state-vector simulator, and no qtDNN surrogate participates in this inference path.

B.3 Backward pass with the qtDNN surrogate (supervised training, no RL)

For gradient-based training we keep the forward topology of Sec. B.2 but replace the non-differentiable $\text{PQC} \rightarrow \mathbf{z}_{\text{q}}$ map by its qtDNN surrogate, yielding the computational graph

$$\mathbf{x} \xrightarrow{f_{\text{Pre}}} \mathbf{q}_{\text{i}} \xrightarrow{f_{\text{qtDNN}}} \hat{\mathbf{z}}_{\text{q}} \xrightarrow{f_{\text{Post}}} \mathbf{y}_{\text{pred}} \xrightarrow{\mathcal{L}(\cdot, y_{\text{true}})} \mathcal{L}_{\text{sup}}.$$

The loss \mathcal{L}_{sup} is task-specific (e.g. MSE or cross-entropy). Because f_{qtDNN} is an ordinary neural network, automatic differentiation supplies $\nabla_{\theta_{\text{Post}}} \mathcal{L}_{\text{sup}}$, $\nabla_{\omega} \mathcal{L}_{\text{sup}}$, and $\nabla_{\theta_{\text{Pre}}} \mathcal{L}_{\text{sup}}$ without invoking the quantum simulator. During the same update step we refine the surrogate itself by a second objective, the BCE in Eq. (6), computed on the cached pair $(\mathbf{q}_{\text{i}}, \mathbf{z}_{\text{q}})$ from the forward PQC evaluation:

$$\omega \leftarrow \omega - \eta_{\text{qt}} \nabla_{\omega} \left(\mathcal{L}_{\text{sup}} + \lambda_{\text{BCE}} \mathcal{L}_{\text{qtDNN}} \right).$$

Thus the qtDNN plays a dual role: it provides differentiable expectation values for end-to-end learning and simultaneously learns to approximate the true quantum channel, all while keeping the backward pass strictly classical and GPU-resident.

B.4 Reinforcement Learning

The hDQNN-TD3's forward pass with RL is already included in the main paper, in Algorithm 1. This section will simply introduce the underlying concepts in higher depth.

B.4.1 Notations and Definitions

- **State and Action Dimensionality:**

$$\begin{aligned} s &\in \mathbb{R}^{n_s} & (\text{the observed state in practice}), \\ a &\in \mathbb{R}^{n_a} & (\text{the action suggested by the actor}). \end{aligned}$$

- **Transitions and Replay Buffer:** At each timestep t , we observe $(s_t, a_t, r_t, s_{t+1}, q_i, q_o)$ where $r_t \in \mathbb{R}$ is the reward, and s_{t+1} is the next state governed by $P(s_{t+1} | s_t, a_t)$. Each 6-tuple

$$(s, a, r, s', q_i, q_o)$$

is stored in a *replay buffer*, \mathcal{M} . During training, we sample mini-batches $\{(s, a, r, s', q_i, q_o)\}$ from \mathcal{M} to update the actor and critic networks.

B.4.2 Actor-Critic Framework

- **Critic Model:**

Let $C : (s, a) \mapsto \hat{R}$ be the critic, parameterized by θ_C . It estimates the expected cumulative reward (or return). We define the one-step temporal-difference (TD) target:

$$R^{\text{target}} = r + \gamma C(s', A(s'; \theta_A)),$$

where $\gamma \in (0, 1)$ is the discount factor, and $A(s'; \theta_A)$ is the actor's action in state s' . The critic loss is:

$$\mathcal{L}_C(\theta_C) = \mathbb{E}_{(s, a, r, s') \sim \mathcal{M}} \left[\left(C(s, a; \theta_C) - (r + \gamma C(s', A(s'; \theta_A))) \right)^2 \right],$$

where \mathcal{M} is the replay buffer.

- **Actor Model (hDQNN):**

The actor $A(s; \theta_A)$ is a hybrid deep quantum neural network that outputs an action a . In particular, it can be decomposed as follows:

$$\mathbf{q}_i = f_{\text{preDNN}}(s; \theta_A),$$

$$\mathbf{q}_o \sim P(\mathbf{q}_o | \mathbf{q}_i) = (\text{Measurement of PQC parameterized by } \mathbf{q}_i),$$

$$a = A(s; \theta_A) = f_{\text{postDNN}}(\mathbf{q}_o, \mathbf{z}_{\text{c-link}}; \theta_A),$$

where $\mathbf{z}_{\text{c-link}}$ indicates possible direct links from the output of f_{preDNN} to the input of f_{postDNN} . The distribution $P(\mathbf{q}_o | \mathbf{q}_i)$ captures the probability of measuring a particular bitstring \mathbf{q}_o on the quantum hardware.

- **Actor Update:**

To update the parameters θ_A of the actor model, we often *maximize* the expected return as estimated by the critic:

$$\mathcal{L}_A(\theta_A) = \mathbb{E}_{s \sim \mathcal{M}} [C(s, A(s; \theta_A); \theta_C)].$$

In practice, gradients $\nabla_{\theta_A} \mathcal{L}_A$ are computed. Here, the qtDNN can be used to approximate the map $\mathbf{q}_i \mapsto \mathbf{q}_o$ locally. This allows batched backpropagation through the classical layers without repeatedly querying the quantum circuit for gradients.

B.5 Forward pass of hDQNN-TD3 (interaction phase)

At training time the hybrid agent interacts with the environment according to the TD3 loop sketched in Algorithm 1 of the main paper. For each environment step t we execute

1. **Actor evaluation.** The current observation s_t is propagated through the hybrid actor exactly as in Sec. B.2, i.e. $s_t \xrightarrow{\text{PreDNN}} \mathbf{q}_{i,t} \xrightarrow{\text{PQC}} \mathbf{z}_{q,t} \xrightarrow{\text{PostDNN}} a_t$. Exploration noise $\varepsilon_t \sim \mathcal{N}(0, \sigma^2 I)$ is then added:

$$\tilde{a}_t = \text{clip}(a_t + \varepsilon_t, a_{\min}, a_{\max}).$$

2. **Environment step.** We execute \tilde{a}_t in the environment, observe r_t , s_{t+1} , done_t and store the transition $(s_t, \tilde{a}_t, r_t, s_{t+1}, \mathbf{q}_{i,t}, \mathbf{z}_{q,t})$ in the replay buffer \mathcal{M} .

Only the genuine PQC is queried during the interaction phase; the qtDNN is *not* used here.

B.6 Backward pass of hDQNN-TD3 (update phase)

Every u environment steps we draw a minibatch $\mathcal{B} \subset \mathcal{D}$ and perform the following updates.

1. **Critic update (twice).** For each transition $(s, a, r, s', \mathbf{q}_i, \mathbf{z}_q) \in \mathcal{B}$ compute the bootstrap target

$$y = r + \gamma \min_{j=0,1} C_j^{\text{tar}}(s', a^{\text{tar}}(s')),$$

where the *target* actor-critic pair on $s' = s_{t+1}$:

$$a^{\text{tar}}(s') = A_{\text{tar}}(s') + \text{clip}(\varepsilon', -c, +c), \quad \varepsilon' \sim \mathcal{N}(0, \sigma'^2 I).$$

then minimise the MSE for both critics C_0, C_1 :

$$\mathcal{L}_{C_j} = \frac{1}{|\mathcal{B}|} \sum_{(s,a) \in \mathcal{B}} (C_j(s, a) - y)^2, \quad j = 0, 1.$$

2. **Actor surrogate update (delayed).** Every $N_A = 2$ critic steps we update the actor parameters θ_A following the original TD3:

1. Replace the non-differentiable mapping $\mathbf{q}_i \mapsto \mathbf{z}_q$ by the qtDNN prediction $\hat{\mathbf{z}}_q = f_{\text{qtDNN}}(\mathbf{q}_i; \omega)$.

2. Construct actions $\hat{a} = f_{\text{PostDNN}}(\hat{\mathbf{z}}_q, \cdot)$ and minimise the deterministic TD3 objective

$$\mathcal{L}_A(\theta_A) = -\frac{1}{|\mathcal{B}|} \sum_{s \in \mathcal{B}} C_0(s, \hat{a}(s)).$$

Autograd now flows through the qtDNN, allowing gradients w.r.t. θ_{Pre} and θ_{Post} without extra PQC calls.

3. qtDNN fitting. On the same minibatch we refine the surrogate by minimising the BCE loss of Eq. (6):

$$\mathcal{L}_{\text{BCE}}(\omega) = \frac{1}{|\mathcal{B}|} \sum_{(\mathbf{q}_i, \mathbf{z}_q) \in \mathcal{B}} \text{BCE}\left(\mathbf{z}_q, f_{\text{qtDNN}}(\mathbf{q}_i; \omega)\right).$$

The qtDNN therefore learns on-the-fly to emulate the quantum circuit while simultaneously providing the actor with differentiable expectation values.

4. Target-network update. Finally we softly update the target networks with rate τ :

$$\phi^{\text{tar}} \leftarrow \tau \phi + (1 - \tau) \phi^{\text{tar}}, \quad \phi \in \{\theta_A, \theta_{C_0}, \theta_{C_1}\}.$$

C Additional graphs and tables

C.1 Extended Ablation

Table 3 shows the extended ablation on Humanoid-v4. Test returns are averaged over the listed seeds. Because each PQC setting can exceed 24 GPU-hours, we could not complete every random seed for every checkpoint before the submission deadline. Where fewer than five seeds are reported (see the ‘‘Seeds’’ column), the missing runs were still in progress; the completed runs are shown to provide early insight rather than to claim definitive rankings.

For coherence purpose, we also display Table 4, which shows the extended ablation on Humanoid-v4 with seed 3 omitted, as it couldn’t run further than 6200 episodes before the submission deadline.

C.2 Detailed Graphs with seeds

Figure 5 juxtaposes four learning curves obtained from an ablation study on the quantum layer’s hyper-parameters. Each subplot displays the 100-episode moving-average return on Humanoid-v4 produced by the hDQNN-TD3 backbone while varying both the number of circuit shots, {100, 1000}, and the number of active qubits, {5, 10}. Every solid, colored trace corresponds to a single random seed; no additional smoothing or confidence band is applied, so the visible oscillations are the raw training dynamics. The comparison indicates that (i) increasing the qubit count from five to ten accelerates early learning only when the shot budget remains low, whereas (ii) allocating more shots generally stabilizes convergence but yields high returns chiefly in the smaller-qubit regime.

D A word on the technical stack: NVIDIA CUDA-Q

We adopted CUDA-Q⁶ as our quantum-simulation engine for one main reason: the GPU is a light weight and agile way to develop and carry out small-scale tests for new model architectures with a small number of qubits involved. Fine-grained quantitative investigations could be carried out easily in this way to understand the behaviors of novel hybrid quantum-classical machine learning architectures by limiting the qubit count, offering direct insights into their foundation of learning and information processing flows. CUDA-Q provides GPU-accelerated tensor-network and state-vector simulators for quick proof-of-concept demonstrations on GPUs. The hDQNN architectures validated in through this could be straightforwardly scaled towards beyond classical large models (with a medium or large qubit count) running on hybrid systems having classical computing resources (CPU/GPU) interconnected with physical (noisy) QPUs.

⁶<https://developer.nvidia.com/cuda-quantum>

Table 3: Extended ablation on Humanoid-v4. Test returns are averaged over 4 – 5 seeds; the right-most column lists the seed indices contributing to each mean.

Ep.	Layer	Shots	Qu.	Mean ret.	Best ret.	Time	PQC calls	Seeds
4 000	FC	0	0	423.0 ± 170.8	603.6	31.5	214 686	0,1,2,3,4
4 000	RBG	0	0	333.6 ± 196.5	545.3	35.7	198 449	0,1,2,3,4
4 000	PQC	100	5	$1\,575.9 \pm 1\,923.4$	4 882.7	515.2	540 138	0,1,2,3,4
4 000	PQC	1 000	5	476.5 ± 149.4	650.8	225.3	280 476	0,1,2,3,4
4 000	PQC	100	10	667.3 ± 442.1	1 453.3	315.2	335 815	0,1,2,3,4
4 000	PQC	1 000	10	556.0 ± 81.7	689.4	265.5	308 709	0,1,2,3,4
6 200	FC	0	0	543.4 ± 243.3	909.4	72.2	423 010	0,1,2,3,4
6 200	RBG	0	0	417.0 ± 131.4	526.2	75.5	366 904	0,1,2,3,4
6 200	PQC	100	5	$2\,014.7 \pm 2\,008.6$	4 342.4	1 596.6	1 387 705	0,1,2,3,4
6 200	PQC	1 000	5	544.8 ± 395.1	1 102.7	467.0	517 611	0,1,2,3,4
6 200	PQC	100	10	$1\,492.3 \pm 2\,191.2$	5 411.2	988.9	959 152	0,1,2,3,4
6 200	PQC	1 000	10	657.0 ± 145.0	841.6	552.6	610 225	0,1,2,3,4
7 000	FC	0	0	693.3 ± 453.1	1 473.0	98.5	515 399	0,1,2,3,4
7 000	RBG	0	0	466.7 ± 106.0	547.2	92.8	438 296	0,1,2,3,4
7 000	PQC	100	5	$2\,139.6 \pm 2\,180.2$	4 962.0	1 935.9	1 756 266	0,1,2,3,4
7 000	PQC	1 000	5	733.1 ± 740.4	1 974.3	612.5	642 867	0,1,2,3,4
7 000	PQC	100	10	532.7 ± 105.6	690.6	678.9	666 056	0,1,2,4
7 000	PQC	1 000	10	710.1 ± 238.6	1 040.6	675.5	744 615	0,1,2,3,4
7 200	FC	0	0	617.5 ± 341.1	1 207.8	108.8	544 790	0,1,2,3,4
7 200	RBG	0	0	414.3 ± 103.0	545.0	99.6	456 050	0,1,2,3,4
7 200	PQC	100	5	$1\,605.0 \pm 2\,202.2$	4 906.6	1 791.9	1 527 037	0,1,2,4
7 200	PQC	1 000	5	$1\,078.5 \pm 1\,517.3$	3 759.2	673.0	692 138	0,1,2,3,4
7 200	PQC	100	10	517.8 ± 95.0	659.2	712.2	694 104	0,1,2,4
7 200	PQC	1 000	10	763.5 ± 335.7	1 277.4	711.9	782 646	0,1,2,3,4
7 700	FC	0	0	$1\,126.1 \pm 1\,467.2$	3 745.5	135.4	621 311	0,1,2,3,4
7 700	RBG	0	0	432.4 ± 97.4	543.2	110.8	500 487	0,1,2,3,4
7 700	PQC	100	5	$1\,402.8 \pm 1\,757.3$	4 031.1	1 943.2	1 688 888	0,1,2,4
7 700	PQC	1 000	5	$1\,121.4 \pm 1\,558.9$	3 868.6	839.3	824 076	0,1,2,3,4
7 700	PQC	100	10	506.6 ± 97.0	624.5	793.6	765 043	0,1,2,4
7 700	PQC	1 000	10	891.8 ± 547.1	1 852.9	805.0	882 668	0,1,2,3,4

During the proof-of-concept trainings on GPU, every forward pass of the PQC is dispatched to the CUDA-Q state-vector simulator in single precision (FP32). The PQC is executed repeatedly with the same parameters over multiple shots. The most probable bit-string from measuring the qubits in the final step of each shot is passed back from the quantum kernel as the output of the quantum layer (in a PQC Call as defined in the main text) to PostDNN. In this process, all classical DNNs and the connected quantum kernel are hosted on one GPU node.

D.1 Hardware and system software.

All experiments were executed independently on a dedicated NVIDIA A100-SXM4 GPU (40 GB HBM2e). The software stack comprised:

- Python 3.12.3;
- PyTorch 2.6.0 built against CUDA 12.4.0;
- Gymnasium 1.1.1 with MuJoCo 3.3.2;
- cuda-q 0.9.1 for GPU-accelerated quantum-circuit simulation NVIDIA [2022].

Table 4: Ablation on Humanoid-v4 with seed 3 still running. Each mean is averaged over the seeds listed in the right-most column.

Ep.	Layer	Shots	Qu.	Mean ret.	Best ret.	Time	PQC calls	Seeds
4 000	FC	0	0	382.7 ± 167.5	603.6	27.4	196 401	0,1,2,4
4 000	RBG	0	0	356.5 ± 219.1	545.3	39.8	210 584	0,1,2,4
4 000	PQC	100	5	$1\,555.4 \pm 1\,923.4$	4 882.7	564.8	574 890	0,1,2,4
4 000	PQC	1 000	5	521.3 ± 128.0	650.8	237.5	302 738	0,1,2,4
4 000	PQC	100	10	470.8 ± 57.1	534.5	291.2	302 948	0,1,2,4
4 000	PQC	1 000	10	568.0 ± 89.2	689.4	258.4	303 057	0,1,2,4
6 200	RBG	0	0	389.7 ± 134.3	521.2	80.4	372 226	0,1,2,4
6 200	FC	0	0	514.3 ± 270.8	909.4	61.1	384 622	0,1,2,4
6 200	PQC	100	5	$1\,432.7 \pm 1\,766.9$	4 075.3	1 489.3	1 196 503	0,1,2,4
6 200	PQC	1 000	5	602.9 ± 430.8	1 102.7	498.4	567 036	0,1,2,4
6 200	PQC	100	10	512.5 ± 52.6	590.5	551.2	557 415	0,1,2,4
6 200	PQC	1 000	10	652.4 ± 167.0	841.6	544.0	593 357	0,1,2,4
7 000	FC	0	0	691.6 ± 523.2	1 473.0	81.9	467 999	0,1,2,4
7 000	RBG	0	0	446.5 ± 110.8	543.4	98.2	440 609	0,1,2,4
7 000	PQC	100	5	$1\,666.9 \pm 2\,201.8$	4 962.0	1 730.9	1 460 228	0,1,2,4
7 000	PQC	1 000	5	837.8 ± 811.1	1 974.3	664.2	711 615	0,1,2,4
7 000	PQC	100	10	532.7 ± 105.6	690.6	678.9	666 056	0,1,2,4
7 000	PQC	1 000	10	698.3 ± 273.8	1 040.6	665.6	724 890	0,1,2,4
7 200	FC	0	0	620.8 ± 393.8	1 207.8	89.8	494 098	0,1,2,4
7 200	RBG	0	0	426.8 ± 114.5	545.0	105.9	458 399	0,1,2,4
7 200	PQC	100	5	$1\,605.0 \pm 2\,202.2$	4 906.6	1 791.9	1 527 037	0,1,2,4
7 200	PQC	1 000	5	$1\,269.5 \pm 1\,681.1$	3 759.2	735.6	770 278	0,1,2,4
7 200	PQC	100	10	517.8 ± 95.0	659.2	712.2	694 104	0,1,2,4
7 200	PQC	1 000	10	768.9 ± 387.4	1 277.4	700.9	761 498	0,1,2,4
7 700	FC	0	0	$1\,253.1 \pm 1\,662.1$	3 745.5	115.1	573 588	0,1,2,4
7 700	RBG	0	0	431.2 ± 112.4	543.2	118.3	504 233	0,1,2,4
7 700	PQC	100	5	$1\,402.8 \pm 1\,757.3$	4 031.1	1 943.2	1 688 888	0,1,2,4
7 700	PQC	1 000	5	$1\,326.7 \pm 1\,720.3$	3 868.6	933.4	927 753	0,1,2,4
7 700	PQC	100	10	506.6 ± 97.0	624.5	793.6	765 043	0,1,2,4
7 700	PQC	1 000	10	945.3 ± 616.5	1 852.9	788.8	855 506	0,1,2,4

D.2 Supplementary figures

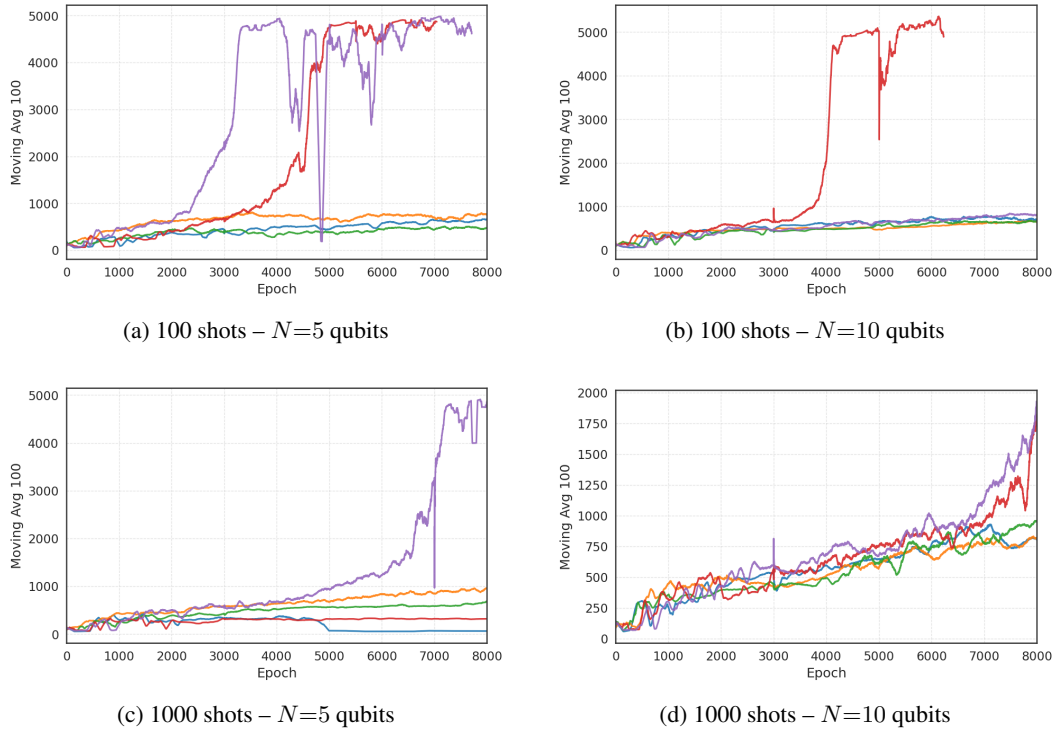


Figure 5: Moving-average (100-episode window) return curves for four PQC configurations. Each colored trace corresponds to one random seed, consistent across the experiments.

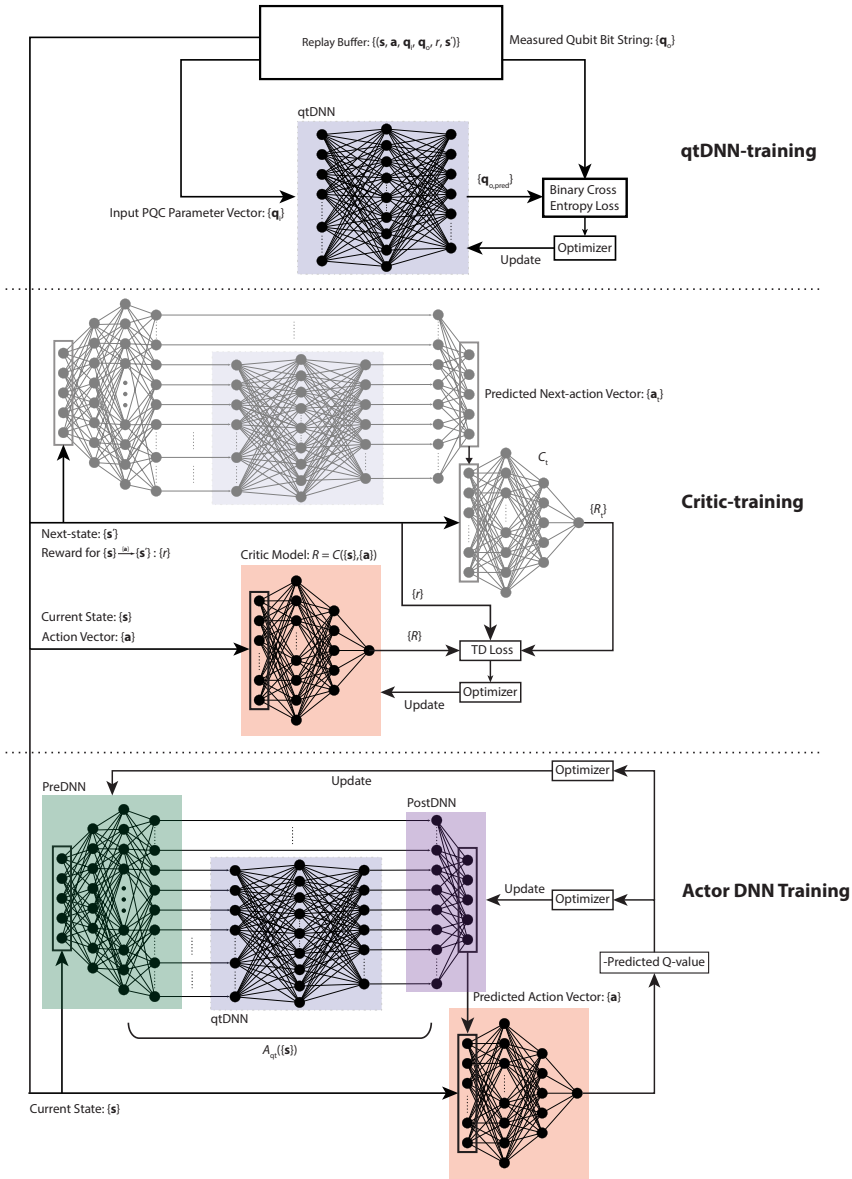


Figure 6: The batched training process flow that incorporates qtDNN training framework for efficiently updating the classical neural layers of the hDQNN model to achieve desired learning goals.